Kinetic energy transfer in compressible homogeneous anisotropic turbulence

Xiaoning Wang ◉,[1,2,3,4] Jianchun Wang ◉,[1,3,4,*] Hui Li,[2] and Shiyi Chen[1,3,4]

[1]*Guangdong Provincial Key Laboratory of Turbulence Research and Applications, Center for Complex Flows and Soft Matter Research, Department of Mechanics and Aerospace Engineering, Southern University of Science and Technology, Shenzhen 518055, China*
[2]*School of Power and Mechanical Engineering, Wuhan University, Wuhan 430072, China*
[3]*Southern Marine Science and Engineering Guangdong Laboratory, Guangzhou 511458, China*
[4]*Guangdong–Hong Kong–Macao Joint Laboratory for Data-Driven Fluid Mechanics and Engineering Applications, Southern University of Science and Technology, Shenzhen 518055, China*

Kinetic energy transfer in compressible homogeneous anisotropic turbulence is studied by numerical simulations of forced anisotropic turbulence (FAT) in a periodic box and homogeneous shear turbulence (HST) at different turbulent Mach numbers M_t and different Taylor Reynolds numbers Re_λ. In both FAT and HST, the subgrid-scale (SGS) kinetic energy flux is dominated by the streamwise component at large scales, and tends to be isotropic at small scales. As the turbulent Mach number increases, the compressibility slightly enhances the anisotropy of SGS kinetic energy flux and viscous dissipation. The redistribution of kinetic energy from the streamwise direction to two transverse directions by pressure-strain mainly occurs at large length scales. The kinetic energy transferred from the streamwise component through the pressure-strain is shared unequally by the other two components in HST, which is different from the situation of FAT. In FAT, as the Taylor Reynolds number increases, the total SGS kinetic energy flux and its positive and negative components tend to a Reynolds number asymptotic state at small scales for $\text{Re}_\lambda \geqslant 105$. In HST, the positive vertical SGS flux of kinetic energy is significantly enhanced by compression motions, causing the vertical SGS flux component to be larger than the streamwise component at small scales. The interscale energy transfer of the solenoidal mode and dilatational mode is studied by employing Helmholtz decomposition. The dilatational kinetic energy of FAT is nearly isotropic, but that of HST is significantly anisotropic. In HST, the dilatational mode obtains energy not only from the solenoidal mode through nonlinear advection, but also from mean shear by the dilatational production. As the turbulent Mach number increases, the nonlinear advection of HST increases first and then decreases. The dilatational production of HST increases monotonically with the turbulent Mach number, providing the main source of kinetic energy to the dilatational mode at high turbulent Mach number $M_t \geqslant 0.46$.

I. INTRODUCTION

The most important feature of turbulent flow is the interscale energy transfer from the large injecting scales down to the dissipative small scales [1,2]. The energy transfer mechanism remains one of the most challenging problems in turbulence theory due to its complex nonlinear and multiscale nature. The interscale energy transfer is also of practical importance for the large-eddy

*wangjc@sustech.edu.cn

simulation (LES), which solves the large-scale structures of turbulence and models the effect of small-scale flow structures on the large-scale flow dynamics by the subgrid-scale stress [3]. In compressible turbulence, the interscale transfer of kinetic energy is more complex due to the strong couplings between the velocity field and thermodynamic fields, as compared to the situation of incompressible turbulence [4–10].

Most investigations of interscale energy transfer in compressible turbulence are focused on homogeneous isotropic turbulence (HIT) [9,11–16]. Kida and Orszag [11] investigated the statistical properties of decaying compressible isotropic turbulence. They reported that the energy exchange between the kinetic energy and internal energy through the pressure-dilatation interaction can be negligible for the case in which the compressive ratios are small. Aluie [12,14] proved that interscale transfer of kinetic energy in compressible turbulence is dominated by local interactions, under the assumption that the pressure-dilatation cospectrum decays at a sufficiently rapid rate. The result was further verified by numerical simulations of both forced and decaying compressible isotropic turbulence [13]. Wang *et al.* [15] investigated kinetic energy transfer in numerical simulation of compressible isotropic turbulence by applying large-scale forces to both solenoidal and dilatational components of the velocity field. They reported that the subgrid-scale (SGS) kinetic energy flux of the dilatational mode is significantly larger than that of the solenoidal mode in the inertial range, due to the effect of sheetlike shock waves of large scale generated in the simulated flow. Wang *et al.* [9] studied the kinetic energy transfer in compressible isotropic turbulence by numerical simulations with solenoidal forcing. They showed that with the increase of the turbulent Mach number, compression motions enhance the positive SGS flux of kinetic energy, and expansion motions enhance the negative SGS flux of kinetic energy. They found that the compressible (or dilatational) mode persistently absorbs kinetic energy from the solenoidal mode through nonlinear advection. Moreover, the kinetic energy of the compressible mode cascades from large scales to small scales through the compressible SGS flux, and is dissipated by viscosity at small scales.

However, in the vast majority of real-world scenarios, the turbulence is significantly anisotropic due to the anisotropic forcing, including the rotating turbulence [17], magnetohydrodynamical turbulence with a background magnetic field [18–20], stratified turbulence [21], and various types of shear turbulent flows [22–25]. In this study we will focus on compressible homogeneous shear turbulence (HST) and forced anisotropic turbulence (FAT) in a periodic box which are two canonical examples of flows exhibiting the anisotropic features of interscale energy transfer. The FAT has no correlation among the velocity components in different directions, making it the simplest anisotropic flow configuration. The previous studies of FAT have been mainly focused on the local isotropy hypothesis [26], the properties of nonlinear interscale couplings in the Fourier-spectral view [27–29], and the anisotropic scaling laws [30,31]. It is crucial to study the anisotropic properties of interscale energy transfer in homogeneous turbulence. The HST can be considered as a bridge between the strongly idealized homogeneous isotropic turbulence and more realistic turbulent shear flows, sharing the natural energy-generation mechanism of shear flows with the simplicity of homogeneity [32–34]. Early papers on interscale energy transfer of HST usually employ bandpass filtering techniques in the spectral space to separate the length scales in the velocity field. Aluie and Eyink [35] pointed out that individual Fourier modes have no physical significance. Summation over logarithmic wave number bands is necessary to a physical description of a turbulent cascade which is resolved both in scale and in space. Recently, Dong *et al.* [34] employed a spatial filtering approach to study the three-dimensional flow structure associated with regions of intense energy fluxes in incompressible homogeneous shear turbulence. Cardesa and Lozano-Durán [36] studied the properties of SGS energy flux with alternative formulations in the filtered kinetic energy equation in three different incompressible flows, namely, statistically steady homogeneous shear turbulence, isotropic turbulence, and plane turbulent channel flow.

The purpose of this paper is to explore the interscale kinetic energy transfer in two compressible homogeneous anisotropic turbulences, including statistically steady homogeneous shear turbulence and forced anisotropic turbulence in a periodic box. Our analysis is mainly focused on the anisotropic nature and the effect of compressibility for the kinetic energy transfer process.

The following section describes the governing equations and computational method. The one-point statistics of the simulated flow are provided in Sec. III. The dynamical equations for the filtered kinetic energy and its solenoidal and dilatational components are derived in Sec. IV. Section V is devoted to the numerical results on interscale transfer of kinetic energy, with particular care on the anisotropy. Finally, conclusions are drawn in Sec. VI.

II. GOVERNING EQUATIONS AND NUMERICAL METHOD

For compressible turbulence, we introduce a set of reference variables to normalize the hydrodynamic and thermodynamic variables, including the reference length L_r, velocity U_r, density ρ_r, pressure $p_r = \rho_r U_r^2$, temperature T_r, energy per unit volume $\rho_r U_r^2$, viscosity μ_r, and thermal conductivity κ_r [4,7]. There are three reference governing parameters: the reference Reynolds number $\mathrm{Re} = \rho_r U_r L_r/\mu_r$, the reference Mach number $M = U_r/c_r$, and the reference Prandtl number $\mathrm{Pr} = \mu_r C_p/\kappa_r$, which is assumed to be equal to 0.7. In addition, the speed of sound is defined by $c_r = \sqrt{\gamma R T}$, where R is the specific gas constant. $\gamma = C_p/C_v$ is the ratio of specific heat at constant pressure C_p to that at constant volume C_v, which is assumed to be equal to 1.4.

The following dimensionless Navier-Stokes equations in conservation form are solved numerically for forced anisotropic turbulence,

$$\frac{\partial \rho}{\partial t} + \frac{\partial (\rho u_k)}{\partial x_k} = 0, \tag{1}$$

$$\frac{\partial (\rho u_i)}{\partial t} + \frac{\partial (\rho u_k u_i)}{\partial x_k} = -\frac{\partial p}{\partial x_i} + \frac{1}{\mathrm{Re}}\frac{\partial \sigma_{ik}}{\partial x_k} + \delta_{1i}F, \tag{2}$$

$$\frac{\partial E}{\partial t} + \frac{\partial [(E+p)u_j]}{\partial x_j} = \frac{1}{\alpha}\frac{\partial}{\partial x_k}\left(\kappa \frac{\partial T}{\partial x_k}\right) + \frac{1}{\mathrm{Re}}\frac{\partial (u_j \sigma_{jk})}{\partial x_k} - \Lambda + \delta_{1j}F u_j, \tag{3}$$

$$p = \rho T/(\gamma M^2), \tag{4}$$

where u_i are fluctuation velocity components, and the indices $i = 1, 2, 3$ denote the three spatial directions represented by x_1, x_2, and x_3, which are the streamwise, vertical, and spanwise directions, respectively. ρ is instantaneous density, p is instantaneous pressure, and T is instantaneous temperature. Here, F is a streamwise large-scale forcing applying to the solenoidal component of the velocity field, and Λ is a large-scale cooling function per unit volume [37]. In general situations, the energy is injected at all scales, such as in buoyancy driven, chemically reacting, and shear turbulence. The artificial large-scale forcing applied here only affect the energy transfer near the forcing scales. This localizing kinetic energy injection to the largest scales is important to enable the study of an intermediate scale range over which inertial processes dominate [14].

The viscous stress σ_{ik} is defined as

$$\sigma_{ik} = 2\mu S_{ik} - \frac{2\mu\theta}{3}\delta_{ik}, \tag{5}$$

in which $S_{ik} = (\partial u_i/\partial x_k + \partial u_k/\partial x_i)/2$ is the strain rate tensor, and $\theta = \partial u_k/\partial x_k$ is the velocity divergence. The total energy per unit volume E is defined as

$$E = \frac{p}{\gamma - 1} + \frac{1}{2}\rho u_i u_i. \tag{6}$$

The temperature-dependent viscosity coefficient and thermal conductivity coefficient are specified by Sutherland's law [38].

In HST, the flow is sustained by a mean velocity field with the form of $U = (Sx_2, 0, 0)$, where $S = \partial U/\partial x_2$ is a uniform shear rate. After the Reynolds decomposition, the dimensionless

TABLE I. Simulation parameters and resulting flow statistics.

Flow type	Re_λ	M_t	N	$\eta/\Delta x$	λ/η	u'	θ'	ω'	S_3	ϵ	$-\langle p\theta \rangle$
FAT1	64	0.91	64	0.65	16.6	2.05	0.97	4.80	−0.43	0.50	4.10×10^{-3}
FAT2	90	0.99	128	0.76	18.4	2.22	1.97	6.87	−0.72	0.53	9.71×10^{-3}
FAT3	105	1.01	256	1.03	19.2	2.25	3.19	9.36	−1.14	0.64	3.49×10^{-2}
FAT4	156	0.40	512	1.01	24.9	2.27	0.46	16.71	−0.51	0.71	3.13×10^{-3}
FAT5	156	0.60	512	0.99	24.9	2.30	2.04	16.86	−0.51	0.74	1.44×10^{-3}
FAT6	155	0.81	512	1.01	24.0	2.30	3.57	16.48	−0.69	0.74	7.99×10^{-4}
FAT7	163	1.00	512	1.05	23.8	2.26	4.79	14.63	−1.25	0.63	3.87×10^{-2}
FAT8	267	1.00	1024	1.04	30.8	2.23	6.67	22.76	−1.29	0.58	1.94×10^{-2}
HST1	145	0.17	512	1.02	21.8	1.48	0.78	12.15	−0.51	0.28	1.57×10^{-3}
HST2	148	0.35	512	0.89	23.8	1.74	3.00	14.25	−0.94	0.41	2.33×10^{-2}
HST3	156	0.46	512	0.91	23.6	1.71	3.30	13.61	−1.05	0.39	2.97×10^{-2}

governing equations for the density, fluctuating velocity, and total energy in a fixed frame of reference are [37,39]

$$\frac{\partial \rho}{\partial t} + \frac{\partial(\rho u_k)}{\partial x_k} + Sx_2\frac{\partial \rho}{\partial x_1} = 0, \tag{7}$$

$$\frac{\partial(\rho u_i)}{\partial t} + \frac{\partial(\rho u_k u_i)}{\partial x_k} + Sx_2\frac{\partial(\rho u_i)}{\partial x_1} + S\rho u_2\delta_{i1} = -\frac{\partial p}{\partial x_i} + \frac{1}{\mathrm{Re}}\frac{\partial \sigma_{ik}}{\partial x_k}, \tag{8}$$

$$\frac{\partial E}{\partial t} + \frac{\partial[(E+p)u_j]}{\partial x_j} + Sx_2\frac{\partial E}{\partial x_1} + \rho Su_1 u_2 = \frac{1}{\alpha}\frac{\partial}{\partial x_k}\left(\kappa\frac{\partial T}{\partial x_k}\right) + \frac{1}{\mathrm{Re}}\frac{\partial(u_j\sigma_{jk})}{\partial x_k} + \frac{S\sigma_{12}}{\mathrm{Re}} - \Lambda. \tag{9}$$

Several new terms appear in the governing equations and the viscous stress σ_{ik} becomes

$$\sigma_{ik} = 2\mu S_{ik} - \frac{2\mu\theta}{3}\delta_{ik} + \mu S(\delta_{i1}\delta_{k2} + \delta_{i2}\delta_{k1}). \tag{10}$$

The numerical simulation has been performed using an in-house simulation code employing a hybrid numerical scheme proposed by Wang et al. [40]. The hybrid scheme combines a seventh-order weighted essentially non-oscillatory (WENO) scheme [41] for the shocklet regions and an eighth-order compact central finite difference scheme [42] for smooth regions. The shock front is identified by spatial points with highly negative local velocity divergence as defined by $\theta < -R_\theta\theta'$, with R_θ set to 3.0, where θ' is the rms value of velocity divergence. The stability and accuracy of the scheme have been demonstrated in previous studies of compressible turbulence [7,9,40,43]. Combined with Rogallo's method [44], the hybrid scheme can be used to simulate the compressible HST in a triply periodic box domain, as shown by Chen et al. [37,45] in recent studies of statistically stationary compressible HST.

The numerical simulations of compressible FAT are performed in a periodic cubic box of $(2\pi)^3$ with a uniform grid. The governing equations of compressible HST are solved in a rectangular domain with side lengths $L_x = 4\pi, L_y = L_z = 2\pi$, and the number of grid points (N) in the x direction is doubled, so that the resolution is essentially the same as FAT. The influence of the geometry of the computational domain for HST was investigated by Sekimoto et al. [33], suggesting that the aspect ratios of streamwise and vertical dimensions to the spanwise dimension should be sufficiently large ($L_x \geqslant 2L_z, L_y \geqslant L_z$) to ensure that the flow statistics become independent of the computational domain. The simulation parameters are summarized in Table I. More details about the numerical algorithm can be found in the papers of Wang et al. [40,46] and Chen et al. [37].

III. GENERAL STATISTICS AND COMPONENT ANISOTROPY

A summary of the relevant one-point statistics are given in Table I for both FAT and HST. The Taylor microscale Reynolds number, Re_λ, and the turbulent Mach number, M_t, are calculated as

$$\text{Re}_\lambda = \text{Re}\frac{\langle\rho\rangle u'\lambda}{\sqrt{3}\langle\mu\rangle}, \quad M_t = M\frac{u'}{\langle\sqrt{T}\rangle}, \tag{11}$$

where $\langle\rangle$ represents the spatial average. Here, the root mean square (rms) value of the velocity is given by $u' = \sqrt{\langle u_1^2 + u_2^2 + u_3^2\rangle}$ and the Taylor microscale is defined by

$$\lambda = \sqrt{\frac{\langle u_1^2 + u_2^2 + u_3^2\rangle}{\langle(\partial u_1/\partial x_1)^2 + (\partial u_2/\partial x_2)^2 + (\partial u_3/\partial x_3)^2\rangle}}. \tag{12}$$

Different numerical simulations of FAT are performed in this study to investigate the effect of the Taylor Reynolds number and turbulent Mach number, respectively. Five Taylor Reynolds numbers ranging from 64 to 267 are considered at a high turbulent Mach number $M_t \approx 1.0$. Four different turbulent Mach numbers of 0.4, 0.6, 0.8, and 1.0 are considered at a Taylor Reynolds number $\text{Re}_\lambda \approx$ 160, corresponding to the different levels of compressibility. For compressible HST, three cases are carried out at turbulent Mach numbers of 0.17, 0.35, and 0.46 for a Taylor Reynolds number close to $\text{Re}_\lambda \approx 150$.

The Kolmogorov length scale is defined by $\eta = [\langle\mu/(\text{Re}\rho)\rangle^3/\langle\epsilon\rangle]^{1/4}$, where the dissipation rate of kinetic energy per unit mass ϵ is defined as $\epsilon = (\sigma_{ij}/\text{Re}/\rho)(\partial u_i/\partial x_j)$. The parameter $\eta/\Delta x$ represents the grid resolution, where Δx denotes the grid spacing in each direction. The resolution parameter $\eta/\Delta x$ is around 1.0 in our simulations which is enough to ensure that the overall statistics are well converged [37,46]. The velocity derivative skewness S_3 is defined by

$$S_3 = \frac{[\langle(\partial u_1/\partial x_1)^3 + (\partial u_2/\partial x_2)^3 + (\partial u_3/\partial x_3)^3\rangle]/3}{\{\langle(\partial u_1/\partial x_1)^2 + (\partial u_2/\partial x_2)^2 + (\partial u_3/\partial x_3)^2\rangle/3\}^{3/2}}. \tag{13}$$

In the two homogeneous anisotropic turbulences, the values of S_3 at different compressibility levels (different M_t) are similar to the typical values of -1.5 to -0.4 in compressible isotropic turbulence [46]. The rms value of velocity divergence and vorticity are computed as $\theta' = \sqrt{\langle\theta^2\rangle}$ and $\omega' = \sqrt{\langle\omega_1^2 + \omega_2^2 + \omega_3^2\rangle}$, respectively. Due to the significant effect of compressibility, the magnitudes of S_3 and θ' increase with Taylor Reynolds number Re_λ and turbulent Mach number M_t. It is found that the rms value of vorticity ω' is sensitive to the change of Taylor Reynolds number, while it is insensitive to turbulent Mach number. Similarly to compressible isotropic turbulence, the conversion rate of kinetic energy into internal energy by the pressure dilatation $-\langle p\theta\rangle$ is much smaller than the viscous dissipation ϵ, which can be attributed to the cancellation between the positive values of $p\theta$ in expansion regions and the negative values of $p\theta$ in compression regions [7,9,47].

The component anisotropy for the velocity, velocity derivatives, and vorticity is presented in Table II. As expected, the rms value of the streamwise velocity fluctuation u_1' is obviously larger than u_2' and u_3', since the energy is all fed from streamwise, where $u_i' = \sqrt{\langle u_i^2\rangle}$. In FAT, u_2' is almost equal to u_3'. In HST, u_2' is slightly smaller than u_3', which is in agreement with previous observations of HST [48] and also resembles that in wall shear turbulence [49].

The rms values of $S_{ii} = \partial u_i/\partial x_i$ (avoiding summation) and ω_i are calculated by $S_{ii}' = \sqrt{\langle S_{ii}^2\rangle}$ and $\omega_i' = \sqrt{\langle\omega_i^2\rangle}$, respectively. The anisotropy level of S_{ii}' and ω_i' is lower than that of velocity, since the velocity gradient is dominated by the small-scale motions of turbulence which has a tendency to be isotropic at very high Reynolds number according to Kolmogorov theory [3]. S_{11}' is a little less than S_{22}' and S_{33}'. ω_1' is smaller than ω_2' and ω_3' at low Taylor Reynolds number, and becomes larger

TABLE II. Component anisotropy statistics in velocity, velocity derivative, and vorticity.

Flow type	Velocity			Velocity derivative			Vorticity		
	u'_1/u'	u'_2/u'	u'_3/u'	S'_{11}	S'_{22}	S'_{33}	ω'_1	ω'_2	ω'_3
FAT1	0.90	0.31	0.31	1.07	1.17	1.16	2.48	2.90	2.89
FAT2	0.87	0.35	0.35	1.76	1.90	1.91	3.94	3.98	3.98
FAT3	0.85	0.38	0.38	2.60	2.74	2.75	5.45	5.39	5.38
FAT4	0.82	0.40	0.40	4.15	4.33	4.33	9.95	9.51	9.47
FAT5	0.81	0.42	0.42	4.32	4.45	4.45	9.97	9.61	9.62
FAT6	0.81	0.41	0.41	4.40	4.53	4.53	9.72	9.39	9.41
FAT7	0.85	0.37	0.37	4.15	4.31	4.28	8.61	8.34	8.38
FAT8	0.85	0.38	0.37	6.42	6.59	6.57	13.34	13.02	13.06
HST1	0.70	0.49	0.52	3.04	3.19	3.18	7.25	6.90	6.89
HST2	0.70	0.49	0.51	3.69	4.14	3.87	8.46	8.11	8.11
HST3	0.71	0.49	0.50	3.57	4.03	3.75	8.08	7.75	7.72

at high Taylor Reynolds numbers. The magnitudes of both S'_{ii} and ω'_i increase significantly as the Taylor Reynolds number increases, and they are insensitive to turbulent Mach number.

IV. DYNAMICAL EQUATIONS FOR FILTERED KINETIC ENERGY AND HELMHOLTZ DECOMPOSITION

A filtering technique can be applied to perform a multiscale analysis of compressible turbulence. For a given field f, a filtered field $\overline{f}$ is defined by

$$\overline{f}(x) \equiv \int d^3 \boldsymbol{r} G_l(\boldsymbol{r}) f(x + \boldsymbol{r}), \tag{14}$$

where $G_l(\boldsymbol{r}) \equiv l^{-3}G_l(\boldsymbol{r}/l)$ is the filter function, and $G_l(\boldsymbol{r})$ is a normalized window function. Here, l is the filter width associated with the wavelength of the smallest scale retained by the filtering operation. The Favre filtered field is defined as $\widetilde{f} \equiv \overline{\rho f}/\overline{\rho}$. A top-hat filter is used in our numerical analysis, which is calculated in one dimension by [50]

$$\overline{f}_i = \frac{1}{4n}\left(f_{i-n} + 2\sum_{j=i-n+1}^{i+n-1} f_j + f_{i+n}\right), \tag{15}$$

where the filter width is $l = 2n\Delta x$.

The equations for the average of the filtered kinetic energy $\widetilde{E}_k = \langle \overline{\rho}\widetilde{u}_i^2/2 \rangle$ in FAT and HST read as [9,16]

$$\frac{\partial \langle \widetilde{E}_k \rangle}{\partial t} = -\langle \Phi_l \rangle - \langle \Pi_l \rangle - \langle D_l \rangle + \langle P_l \rangle, \tag{16}$$

$$\frac{\partial \langle \widetilde{E}_k \rangle}{\partial t} = -\langle \Phi_l \rangle - \langle \Pi_l \rangle - \langle \Pi_l^m \rangle - \langle D_l \rangle + \langle P_l \rangle. \tag{17}$$

Here, Φ_l is the large-scale pressure-strain term, Π_l is the SGS kinetic energy flux, D_l is the viscous dissipation term, and P_l is the energy production term. There is an extra term Π_l^m in Eq. (17) for HST, which represents the kinetic energy transfer due to interaction between the filtered and mean

flow. These terms are defined as

$$\Phi_l \equiv -\overline{p}\widetilde{S}_{ii}, \tag{18}$$

$$\Pi_l \equiv -\overline{\rho}\widetilde{\tau}_{ij}\frac{\partial \widetilde{u}_i}{\partial x_j}, \tag{19}$$

$$D_l \equiv \frac{\overline{\sigma}_{ij}}{\text{Re}}\frac{\partial \widetilde{u}_i}{\partial x_j}, \tag{20}$$

$$\Pi_l^m \equiv -\overline{\rho}(\widetilde{u_i U} - \widetilde{u}_i\widetilde{U})\frac{\partial \widetilde{u}_i}{\partial x_1}, \tag{21}$$

and

$$P_l \equiv \widetilde{u}_i\delta_{1i}\overline{F} \tag{22}$$

or

$$P_l \equiv -S\overline{\rho}\delta_{i1}\widetilde{u}_i\widetilde{u}_2 \tag{23}$$

for FAT and HST, respectively. Here, the subgrid-scale (SGS) stress is $\overline{\rho}\widetilde{\tau}_{ij} = \overline{\rho}(\widetilde{u_i u_j} - \widetilde{u}_i\widetilde{u}_j)$. It is straightforward to obtain the equations for three components of kinetic energy by avoiding summation convention over repeated index i in Eqs. (16) and (17). This yields

$$\frac{\partial \langle\widetilde{E}_{k,i}\rangle}{\partial t} = -\langle\Phi_{l,i}\rangle - \langle\Pi_{l,i}\rangle - \langle D_{l,i}\rangle + \langle P_{l,i}\rangle, \tag{24}$$

$$\frac{\partial \langle\widetilde{E}_{k,i}\rangle}{\partial t} = -\langle\Phi_{l,i}\rangle - \langle\Pi_{l,i}\rangle - \langle\Pi_{l,i}^m\rangle - \langle D_{l,i}\rangle + \langle P_{l,i}\rangle, \tag{25}$$

where $i = 1, 2, 3$. The Reynolds shear stress in HST is nonzero. The equation for the average of large-scale Reynolds shear stress reads

$$\frac{\partial}{\partial t}\langle\overline{\rho}\widetilde{u}_1\widetilde{u}_2\rangle = -\langle\Phi_{l,12}\rangle - \langle\Pi_{l,12}\rangle - \langle\Pi_{l,12}^m\rangle - \langle D_{l,12}\rangle + \langle P_{l,12}\rangle, \tag{26}$$

where $P_{l,12} = -S\langle\overline{\rho}\widetilde{u}_2\widetilde{u}_2\rangle$ is the production term, $\Phi_{l,12} = 2\langle\overline{p}\widetilde{S}_{12}\rangle$ is the large-scale pressure-strain term, $\Pi_{l,12}$ and $\Pi_{l,12}^m$ is the kinetic energy flux, and $D_{l,12}$ is the viscous dissipation term.

A filtered density-weighted variable can be introduced as $\widetilde{\boldsymbol{w}} = \sqrt{\overline{\rho}}\widetilde{\boldsymbol{u}}$. Helmholtz decomposition of the $\widetilde{\boldsymbol{w}}$ yields $\widetilde{\boldsymbol{w}} = \widetilde{\boldsymbol{w}}^s + \widetilde{\boldsymbol{w}}^d$, where $\widetilde{\boldsymbol{w}}^s$ and $\widetilde{\boldsymbol{w}}^d$ are the solenoidal and dilatational components, respectively. Take HST, for example; the two components of the filtered density-weighted variable satisfy the following relations: $\nabla \cdot \widetilde{\boldsymbol{w}}^s = 0$ and $\nabla \times \widetilde{\boldsymbol{w}}^d = 0$. The filtered equation for the average of the solenoidal (or dilatational) component of the large-scale kinetic energy is [9,16]

$$\frac{\partial}{\partial t}\left\langle\frac{1}{2}\left(\widetilde{w}_i^X\right)^2\right\rangle = \langle A_l^X\rangle + \langle P_l^X\rangle - \langle\Phi_l^X\rangle - \langle\Pi_l^X\rangle - \langle\Pi_l^{m,X}\rangle - \langle D_l^X\rangle. \tag{27}$$

Here, $X = s, d$. A_l^X is the nonlinear advection term. Φ_l^X is the large-scale pressure-dilatation term. Π_l^X is the SGS kinetic energy flux. D_l^X is the viscous dissipation term. These terms are defined as

$$A_l^X \equiv -\widetilde{w}_i^X\left(\widetilde{u}_j\frac{\partial \widetilde{w}_i}{\partial x_j} + \frac{\widetilde{w}_i}{2}\frac{\partial \widetilde{u}_j}{\partial x_j} + \widetilde{U}\frac{\partial \widetilde{w}_i}{\partial x_1}\right), \tag{28}$$

$$P_l^X \equiv -\widetilde{w}_i^X S\widetilde{w}_2\delta_{i1}, \tag{29}$$

$$\Phi_l^X \equiv -\overline{p}\frac{\partial}{\partial x_i}\left(\frac{\widetilde{w}_i^X}{\sqrt{\overline{\rho}}}\right), \tag{30}$$

$$\Pi_l^X \equiv -\overline{\rho}(\widetilde{u_i u_j} - \widetilde{u}_i\widetilde{u}_j)\frac{\partial}{\partial x_j}\left(\frac{\widetilde{w}_i^X}{\sqrt{\overline{\rho}}}\right), \tag{31}$$
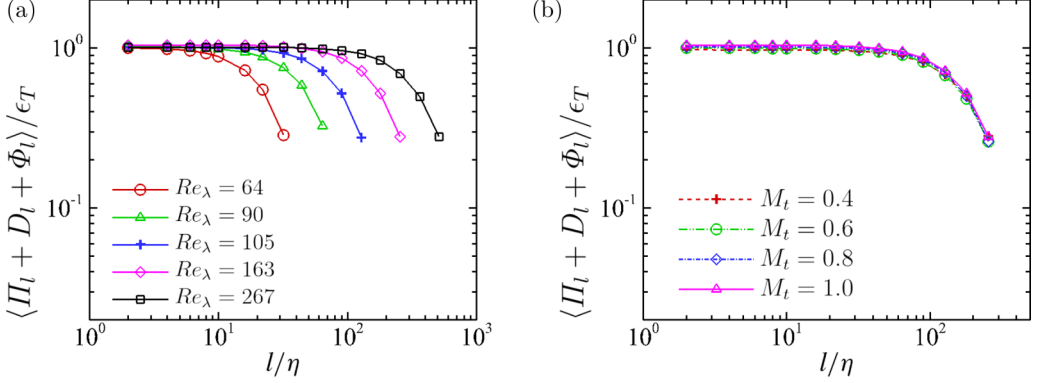
(a)

(b)

FIG. 1. Average of overall kinetic energy transfer: (a) at Taylor Reynolds numbers $Re_\lambda = 64, 90, 105, 163, 267$ for $M_t \approx 1.0$; (b) at turbulent Mach numbers $M_t = 0.4, 0.6, 0.8, 1.0$ for $Re_\lambda \approx 160$.

$$\Pi_l^{m,X} \equiv -\overline{\rho}(\widetilde{u_i U} - \widetilde{u}_i \widetilde{U})\frac{\partial}{\partial x_1}\left(\frac{\widetilde{w}_i^X}{\sqrt{\overline{\rho}}}\right), \tag{32}$$

$$D_l^X \equiv \frac{\overline{\sigma}_{ij}}{Re}\frac{\partial}{\partial x_j}\left(\frac{\widetilde{w}_i^X}{\sqrt{\overline{\rho}}}\right). \tag{33}$$

It is straightforward to derive the following relations: $\langle A_l^s + A_l^d \rangle = 0$, $\Phi_l^s + \Phi_l^d = \Phi_l$, $\Pi_l^s + \Pi_l^d = \Pi_l$, and $D_l^s + D_l^d = D_l$.

V. NUMERICAL RESULTS

A. Forced anisotropic turbulence in a periodic box

1. Effect of large-scale forcing

In Fig. 1(a), we plot the average of overall kinetic energy transfer at Taylor Reynolds numbers $Re_\lambda = 64, 90, 105, 163, 267$ for $M_t \approx 1.0$. The energy transfer terms are normalized by the total dissipation of kinetic energy $\epsilon_T = \epsilon - \langle p\theta \rangle$. In general, kinetic energy is injected at large scales in the streamwise direction, redistributed to vertical and spanwise directions, transferred gradually to smaller scales, and dissipated finally by viscosity at small scales which are close to the Kolmogorov length scale. Since large-scale external forcing is applied only in the streamwise direction, the overall kinetic energy transfers in the vertical and spanwise directions are zero, and those for the total kinetic energy and streamwise component coincide with each other. It is shown that the effect of forcing is focused on the relatively large scales. As the Taylor Reynolds number increases, there is an increase of the forcing scale, giving rise to a wider scale range where the normalized total kinetic energy transfer is nearly equal to 1. The average of overall kinetic energy transfer at turbulent Mach numbers $M_t = 0.4, 0.6, 0.8, 1.0$ for $Re_\lambda \approx 160$ is shown in Fig. 1(b). The overall kinetic energy transfer decreases rapidly as the filter width l/η increases from 100, suggesting that the effect of large-scale external forcing is negligible at scales $l/\eta \leqslant 100$ for $Re_\lambda \approx 160$. Similarly to the results in compressible isotropic turbulence by Wang et al. [9], the averages of the energy transfer terms in FAT remain insensitive to turbulent Mach number; thus they are presented only for the case FAT7 in the rest of this section for brevity.

2. Viscous dissipation

The average of viscous dissipation at turbulent Mach number $M_t = 1.0$ and at Taylor Reynolds number $Re_\lambda = 163$ is shown in Fig. 2(a). The viscous dissipation of all three components is of
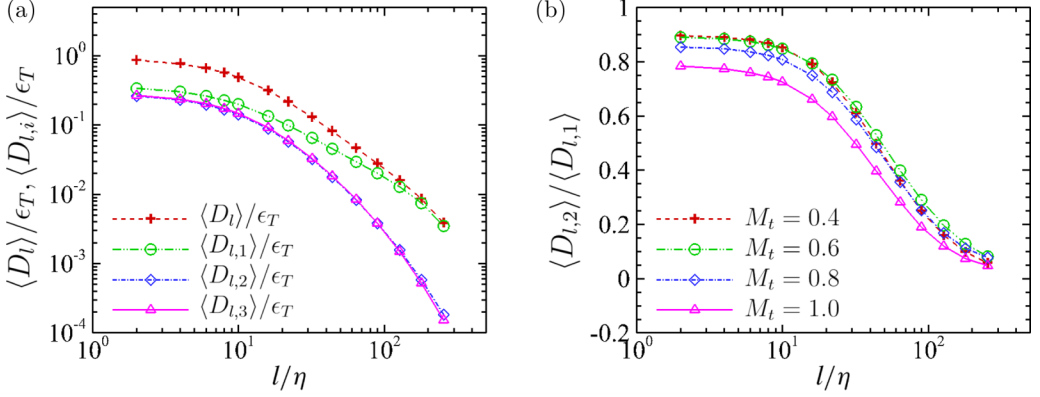
FIG. 2. (a) Average of viscous dissipation terms $\langle D_l \rangle / \epsilon_T$ and $\langle D_{l,i} \rangle / \epsilon_T$ at $M_t = 1.0$ and $\mathrm{Re}_\lambda = 163$. (b) Ratio of transverse to streamwise components of viscous dissipation $\langle D_{l,2} \rangle / \langle D_{l,1} \rangle$ at $M_t = 0.4, 0.6, 0.8, 1.0$ and $\mathrm{Re}_\lambda \approx 160$.

great importance, $\langle D_{l,i} \rangle \approx 0.33 \langle D_l \rangle$, at small scales $l/\eta \leqslant 10$, and decays rapidly at different rates as the filter width increases from 10. It appears that the dissipation processes are anisotropic at larger scales. As seen in Fig. 2(b), with the decrease of the filter scale, the ratio of transverse to streamwise components of viscous dissipation increases from zero at larger scales to more than 0.8 at small scales. The anisotropy at small scales is primarily due to incomplete recovery of local isotropy at finite Taylor Reynolds number. As turbulent Mach number increases, the compressibility slightly increases the anisotropy of viscous dissipation.

The averages of viscous dissipation at different Taylor Reynolds numbers are shown in Figs. 3(a)–3(c) for $M_t \approx 1.0$. As the Taylor Reynolds number increases, the total viscous dissipation $\langle D_l \rangle$ and the streamwise viscous dissipation component approach a Reynolds number asymptotic state where $\langle D_l \rangle$ exhibits a scaling behavior of $(l/\eta)^{-1.5}$ and $\langle D_{l,1} \rangle$ exhibits a scaling behavior of $(l/\eta)^{-1.2}$ at large scales $l/\eta \geqslant 20$. The Reynolds number dependency of the transverse viscous dissipation component is more significant in our numerical simulations. At high Taylor Reynolds numbers, the three viscous dissipation components are approximate to $\epsilon_T/3$ due to the local isotropy of the viscous dissipation process at small filter width. The anisotropy at small scales decreases rapidly as the Taylor Reynolds number increases, which is also shown in Fig. 3(d) for $M_t \approx 1.0$.

3. Large-scale pressure-strain term

The average of large-scale pressure-strain at turbulent Mach number $M_t = 1.0$ and at Taylor Reynolds number $\mathrm{Re}_\lambda = 163$ is shown in Fig. 4(a). The total pressure-strain term $\langle \Phi_l \rangle = \langle p\theta \rangle$ accounts for the net conversion of kinetic energy into internal energy by the pressure dilatation, which is negligibly small due to the cancellation between compression and expansion works. The streamwise component $\langle \Phi_{l,1} \rangle$ is positive, while the two transverse components $\langle \Phi_{l,2} \rangle$ and $\langle \Phi_{l,3} \rangle$ are negative almost everywhere. Considering that no production occurs in the two transverse directions, the pressure-strain components redistribute energy from the streamwise direction to two transverse directions. As seen in Fig. 4(b), the ratio of transverse to streamwise components of pressure-strain approximately equals 0.5 at different length scales, indicating that energy loss from the streamwise component is shared equally by the two transverse components. This redistribution process mainly occurs at large scales $l/\eta \geqslant 10$.

In Figs. 4(c) and 4(d), we plot the root mean square (rms) values of pressure-strain, defined as $\Phi_l' = \sqrt{\langle (\Phi_l - \langle \Phi_l \rangle)^2 \rangle}$, at turbulent Mach numbers $M_t = 0.4, 0.6, 0.8, 1.0$. Φ_l'/ϵ_T and $\Phi_{l,i}'/\epsilon_T$
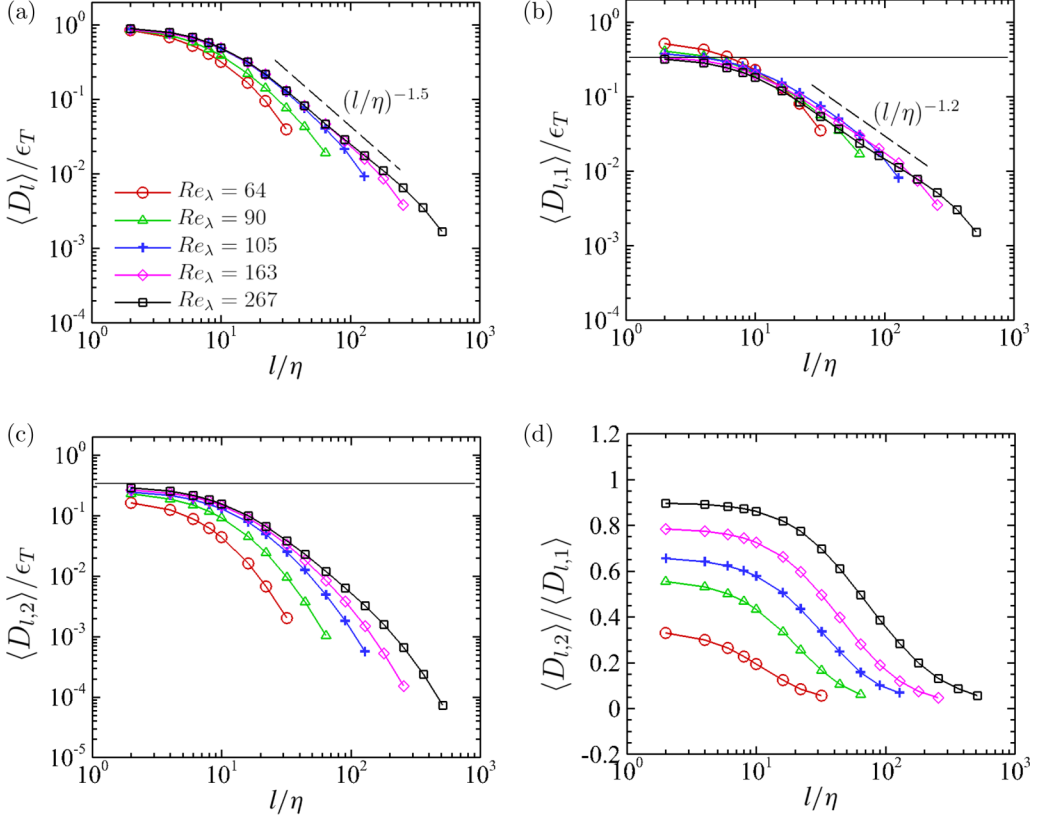
FIG. 3. Average of viscous dissipation and ratio of transverse to streamwise components of viscous dissipation at different Taylor Reynolds numbers $Re_\lambda = 64, 90, 105, 163, 267$ for $M_t \approx 1.0$: (a) $\langle D_l \rangle / \epsilon_T$; (b) $\langle D_{l,1} \rangle / \epsilon_T$; (c) $\langle D_{l,2} \rangle / \epsilon_T$; (d) $\langle D_{l,2} \rangle / \langle D_{l,1} \rangle$.

become larger as the filter width l/η decreases. It is interesting to observe that Φ'_l / ϵ_T is nearly constant at the smallest scale for moderate and high turbulent Mach numbers $M_t \geqslant 0.6$. Since $\langle \Phi_l \rangle$ is negligibly small, Φ'_l can be well approximated by $\sqrt{\langle (\Phi_l)^2 \rangle} \approx \overline{p} \theta'_l$. The ideal gas equation of state [Eq. (4)] indicates that the spatial average pressure is nearly proportional to M_t^{-2}. Consequently, the constant behavior of Φ'_l / ϵ_T at the smallest scale indicates that θ'_l is almost proportional to M_t^2 at the smallest scale when $M_t \geqslant 0.6$. The rms values of all three pressure-strain components $\Phi'_{l,i} \approx \overline{p} (\partial \widetilde{u}_i / \partial x_i)'$ are consistent with each other and are nearly proportional to M_t^{-2}, since $(\partial \widetilde{u}_i / \partial x_i)'$ is nearly independent of M_t, as presented in Table II.

The averages of large-scale pressure-strain at different Taylor Reynolds numbers are shown in Fig. 5(a) for $M_t \approx 1.0$. As the Taylor Reynolds number increases, the loss of streamwise energy by pressure-strain approaches $\langle \Phi_{l,1} \rangle = 2/3\epsilon_T$, and the gain of transverse components approaches $1/3\epsilon_T$. This observation is consistent with previous theoretical analysis of the pressure-strain in incompressible homogeneous shear turbulence [48]. In Fig. 5(b), the filter width l is normalized by the maximum turbulent length scale $l_{\max} = N/2$ that is determined by the domain size. It is interesting to find that the average of large-scale pressure-strain is nearly independent of Re_λ at large scales, indicating that the energy redistribution process is self-similar. The equality of energy redistribution into transverse components by the pressure-strain process holds at different Taylor Reynolds numbers, as shown in Fig. 5(c). Φ'_l and $\Phi'_{l,i}$ are close to each other and increase as the Taylor Reynolds number increases, which is consistent with the fact that θ'_l and $(\partial \widetilde{u}_i / \partial x_i)'_l$ (no
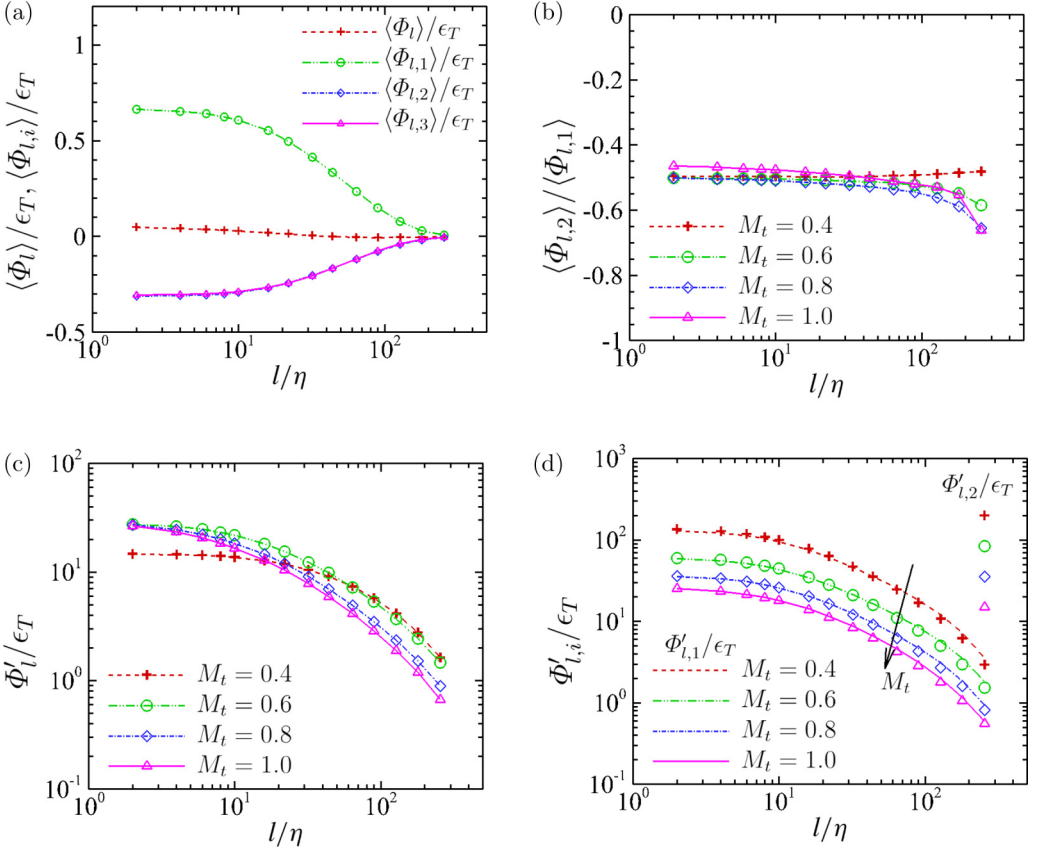
FIG. 4. (a) Average of pressure-strain terms at $Re_\lambda = 163$ and $M_t = 1.0$. (b) Ratio of transverse to streamwise components of pressure-strain terms at $M_t = 0.4, 0.6, 0.8, 1.0$ for $Re_\lambda \approx 160$. The rms values of (c) Φ_l and (d) $\Phi_{l,i}$ at $M_t = 0.4, 0.6, 0.8, 1.0$ for $Re_\lambda \approx 160$.

summation on i, $i = 1, 2, 3$) are similar to each other and both enhanced by Re_λ, as presented in Table II ($\Phi'_{l,2}$ is omitted for brevity).

4. SGS kinetic energy flux

The average of the SGS flux of kinetic energy at turbulent Mach number $M_t = 1.0$ and at Taylor Reynolds number $Re_\lambda = 163$ is shown in Fig. 6(a). The SGS kinetic energy flux $\langle \Pi_l/\epsilon_T \rangle$ is close to 1.0 at scales $30 \leqslant /\eta \leqslant 100$ and dominated by the streamwise component $\langle \Pi_{l,1}/\epsilon_T \rangle$ at large scales. The peak of the streamwise SGS flux component occurs at scale $l/\eta \approx 100$, while the peaks of the two transverse SGS flux components occur at smaller scale $l/\eta \approx 20$ with much lower magnitude. The anisotropy of the SGS flux decreases with the decreases of filter width, as presented in Fig. 6(b); meanwhile, it is strengthened by compressibility as turbulent Mach number increases. The ratio of transverse to streamwise components of SGS flux is less than 0.8 at small scales, indicating that the anisotropy of SGS flux is stronger than that of viscous dissipation. The rms value of SGS flux is defined as $\Pi'_l = \sqrt{\langle (\Pi_l - \langle \Pi_l \rangle)^2 \rangle}$. At relatively small scales $l/\eta < 10$, Π'_l and $\Pi'_{l,i}$ become larger as turbulent Mach number increases, as shown in Fig. 7, which indicates that the compressibility effect will enhance the local transfer of kinetic energy by the SGS stress. It is worth noting that at larger scales $l/\eta > 10$, Π'_l and $\Pi'_{l,1}$ slightly increase with turbulent Mach number, while $\Pi'_{l,2}$ decreases slightly with turbulent Mach number.
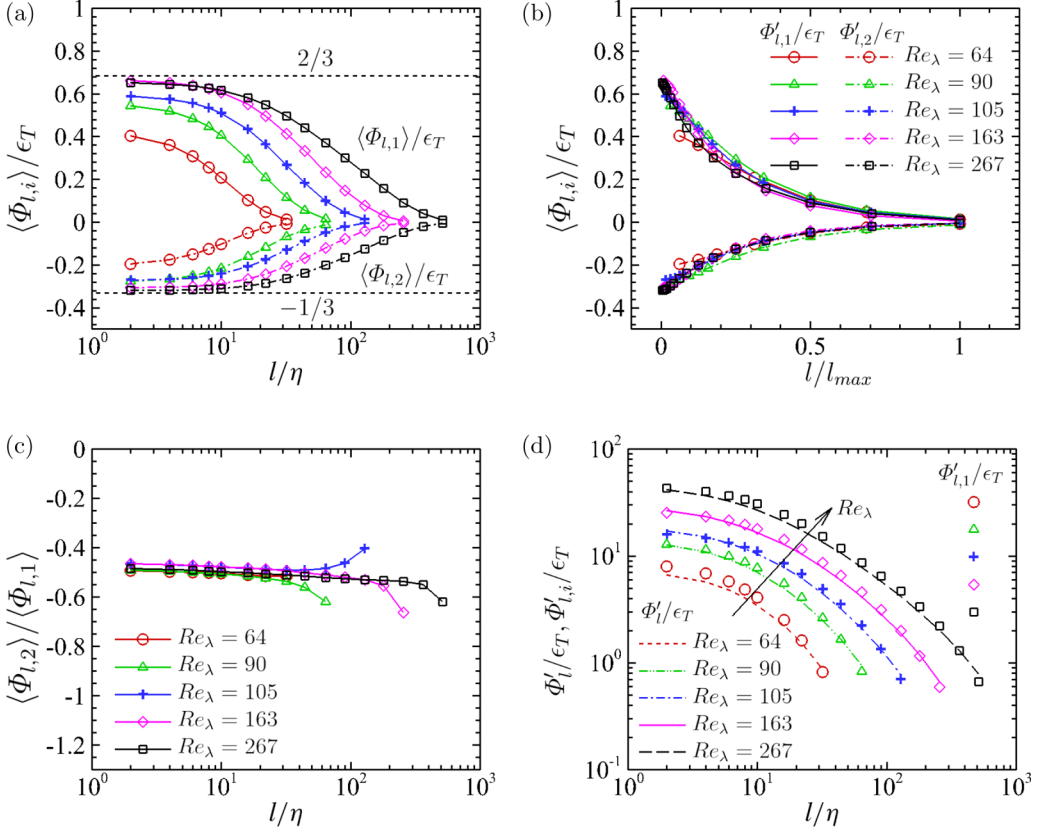
FIG. 5. (a) Average of pressure-strain terms, (b) average of pressure-strain terms versus l/l_{max}, (c) ratio of transverse to streamwise components of pressure-strain, and (d) rms values of pressure-strain at different Taylor Reynolds numbers $Re_\lambda = 64, 90, 105, 163, 267$ for $M_t \approx 1.0$.

The averages of SGS kinetic energy flux at different Taylor Reynolds numbers are shown in Figs. 8(a)–8(c) for $M_t \approx 1.0$. The corresponding scales of the peak values of total SGS flux $\langle \Pi_l \rangle / \epsilon_T$ and SGS flux components $\langle \Pi_{l,i} \rangle / \epsilon_T$ become larger as the Taylor Reynolds number increases, and the peak of $\langle \Pi_l \rangle / \epsilon_T$ is always located between peaks of $\langle \Pi_{l,1} \rangle / \epsilon_T$ and $\langle \Pi_{l,2} \rangle / \epsilon_T$. The peak values of $\langle \Pi_l \rangle / \epsilon_T$ and $\langle \Pi_{l,2} \rangle / \epsilon_T$ increase monotonically with the Taylor Reynolds number, while the peak value of $\langle \Pi_{l,1} \rangle / \epsilon_T$ increases for $Re_\lambda < 160$ and then slightly decreases at $Re_\lambda = 267$. It is worth noting that $\langle \Pi_l \rangle / \epsilon_T$ exhibits Reynolds number similarity at small scale $l/\eta < 30$ for high Taylor Reynolds numbers. This Reynolds number similarity indicates that the universal statistical property of the kinetic energy transfer at small scales starts to appear for Re_λ approximately greater than 150, and the scale range for the universal statistics increases gradually with Taylor Reynolds number. The anisotropy of SGS flux decreases as the Taylor Reynolds number increases, as shown in Fig. 8(d). We speculate that the peak values of all three normalized SGS flux components may gradually approach $1/3$ as the Taylor Reynolds number increases, which is to say that the SGS flux becomes more isotropic in the inertial range with the increase of Taylor Reynolds number.

The probability density function (PDF) of the normalized SGS kinetic energy flux at two Taylor Reynolds numbers $Re_\lambda = 105$ and 267 for a high turbulent Mach number $M_t = 1.0$ is shown in Fig. 9. The inverse kinetic energy flux from small scales to large scales is demonstrated by the negative side of the PDF. The PDF of SGS flux is skewed to the positive value, indicating that the
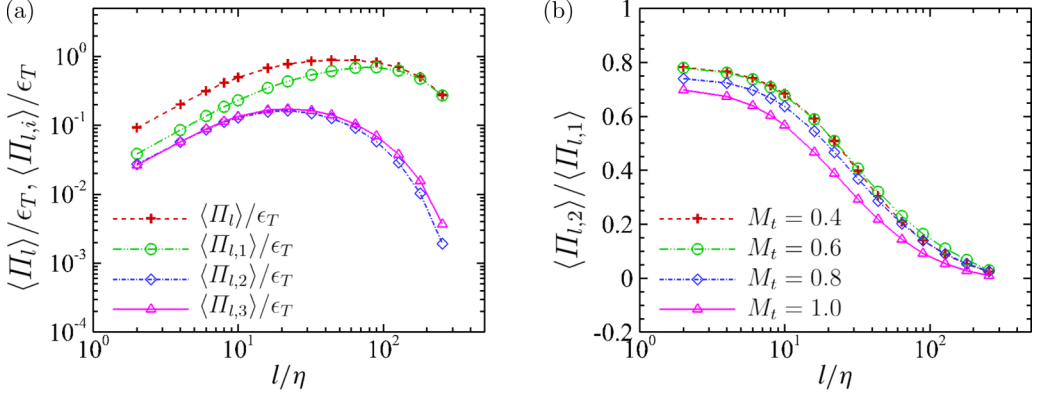
FIG. 6. (a) Average of SGS flux at $\mathrm{Re}_\lambda = 163$ and $M_t = 1.0$. (b) Ratio of transverse to streamwise components of SGS flux at turbulent Mach numbers $M_t = 0.4, 0.6, 0.8, 1.0$ for $\mathrm{Re}_\lambda \approx 160$.

kinetic energy transfer by the SGS stress has a tendency to be from large scales to small scales. We observe that the two tails of the PDF become longer at smaller filter width l and at larger Taylor Reynolds number Re_λ, particularly for the right tail. The PDF tails of $\Pi_{l,2}/\epsilon_T$ are much shorter
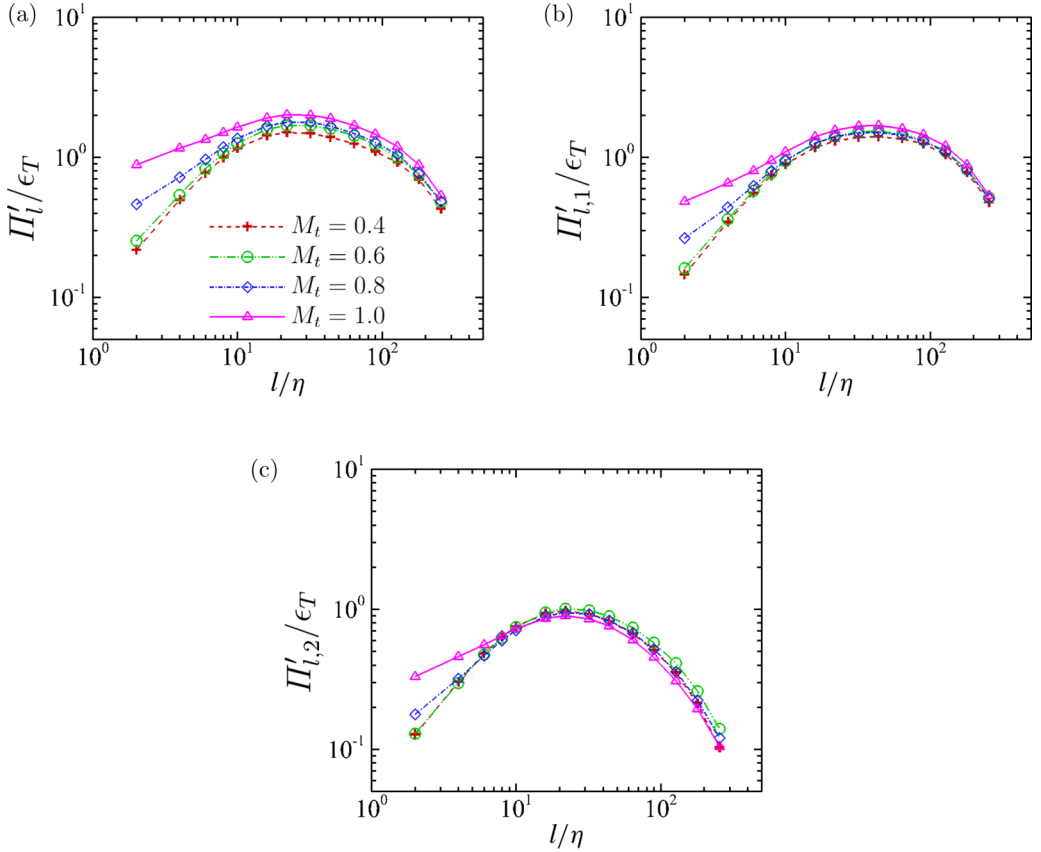
FIG. 7. The rms values of SGS flux at turbulent Mach numbers $M_t = 0.4, 0.6, 0.8, 1.0$ for $\mathrm{Re}_\lambda \approx 160$. (a) Π_l'; (b) $\Pi_{l,1}'$; (c) $\Pi_{l,2}'$.
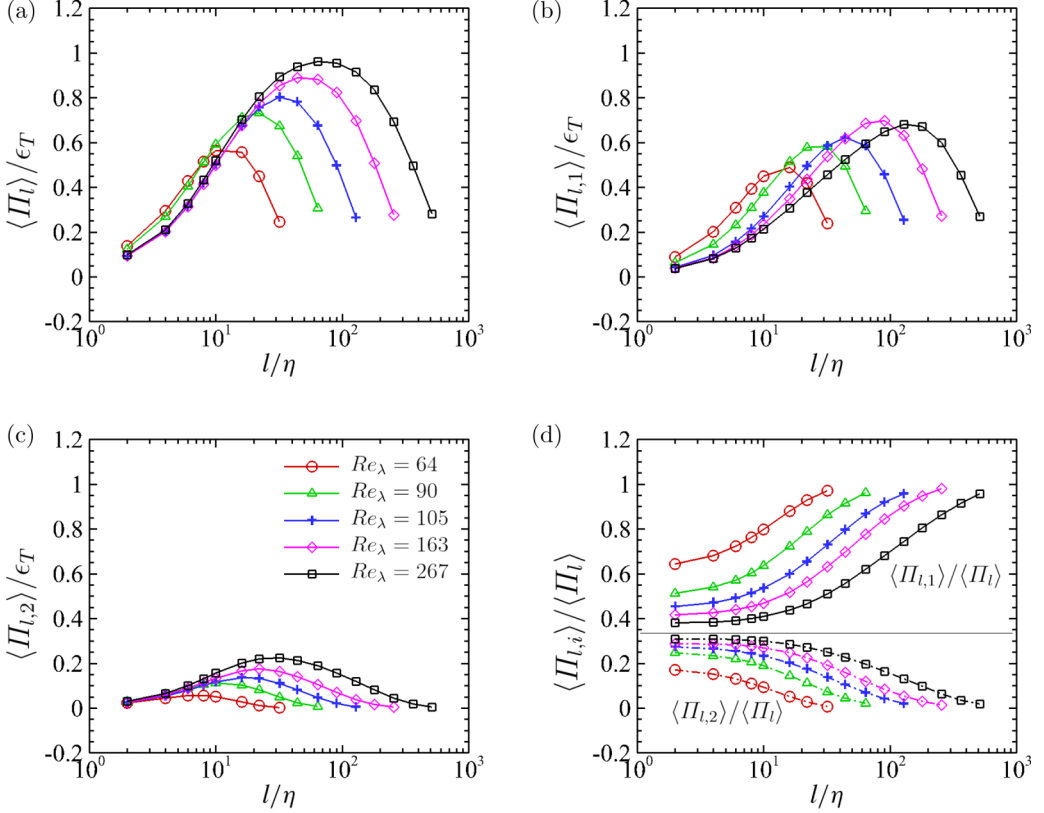
FIG. 8. Average of SGS flux terms and normalized streamwise and transverse components of SGS flux at different Taylor Reynolds numbers $Re_\lambda = 64, 90, 105, 163, 267$ for $M_t \approx 1.0$. (a) $\langle \Pi_l \rangle / \epsilon_T$; (b) $\langle \Pi_{l,1} \rangle / \epsilon_T$; (c) $\langle \Pi_{l,2} \rangle / \epsilon_T$; (d) $\langle \Pi_{l,i} \rangle / \langle \Pi_l \rangle$.

than those of Π_l / ϵ_T and $\Pi_{l,1} / \epsilon_T$. For brevity, the PDFs of SGS flux at different turbulent Mach number are not presented here as the effect of compressibility is qualitatively similar to the situation of compressible isotropic turbulence [9].

We decompose the SGS kinetic energy flux Π_l into positive and negative parts, which are defined as $\Pi_l^+ = 1/2(\Pi_l + |\Pi_l|)$ and $\Pi_l^- = 1/2(\Pi_l - |\Pi_l|)$, respectively. The positive part Π_l^+ represents the direct transfer of kinetic energy from large scales to small scales. In contrast, the negative part Π_l^- represents the inverse transfer of kinetic energy from small scales to large scales, i.e., the backscatter of kinetic energy. The normalized averages of the positive and negative components of SGS flux are shown in Fig. 10. As the turbulent Mach number increases, the magnitudes of $\langle \Pi_l^+ \rangle / \epsilon_T$ and $\langle \Pi_l^- \rangle / \epsilon_T$ become larger, demonstrating the significant effect of compressibility on the SGS energy transfer. Particularly, the SGS backscatter of total kinetic energy becomes more important at higher turbulent Mach numbers. It is shown that $\langle \Pi_{l,1}^+ \rangle / \epsilon_T$ and $\langle \Pi_{l,1}^- \rangle / \epsilon_T$ are less affected by turbulent Mach number. Moreover, the positive and negative components of $\langle \Pi_{l,2} \rangle / \epsilon_T$ and $\langle \Pi_{l,3} \rangle / \epsilon_T$ are nearly independent of turbulent Mach number, as can be seen in Fig. 10.

The averages of the positive and negative components of SGS flux at different Taylor Reynolds numbers are shown in Fig. 11 for $M_t \approx 1.0$. As expected, the behaviors of $\langle \Pi_l^+ \rangle / \epsilon_T$ and $\langle \Pi_{l,i}^+ \rangle / \epsilon_T$ are similar to those of $\langle \Pi_l \rangle / \epsilon_T$ and $\langle \Pi_{l,i} \rangle / \epsilon_T$ (see Fig. 8), respectively. It is worth noting that $\langle \Pi_l^- \rangle / \epsilon_T$ shows Reynolds number similarity at larger extent of scale $l/\eta < 100$ and at higher Taylor Reynolds number. Moreover, $\langle \Pi_{l,1}^- \rangle / \epsilon_T$ also shows Reynolds number similarity. The peak value of $\langle \Pi_{l,2}^- \rangle / \epsilon_T$ increases with the Taylor Reynolds number and exceeds that of $\langle \Pi_{l,1}^- \rangle / \epsilon_T$ for $Re_\lambda > 150$.
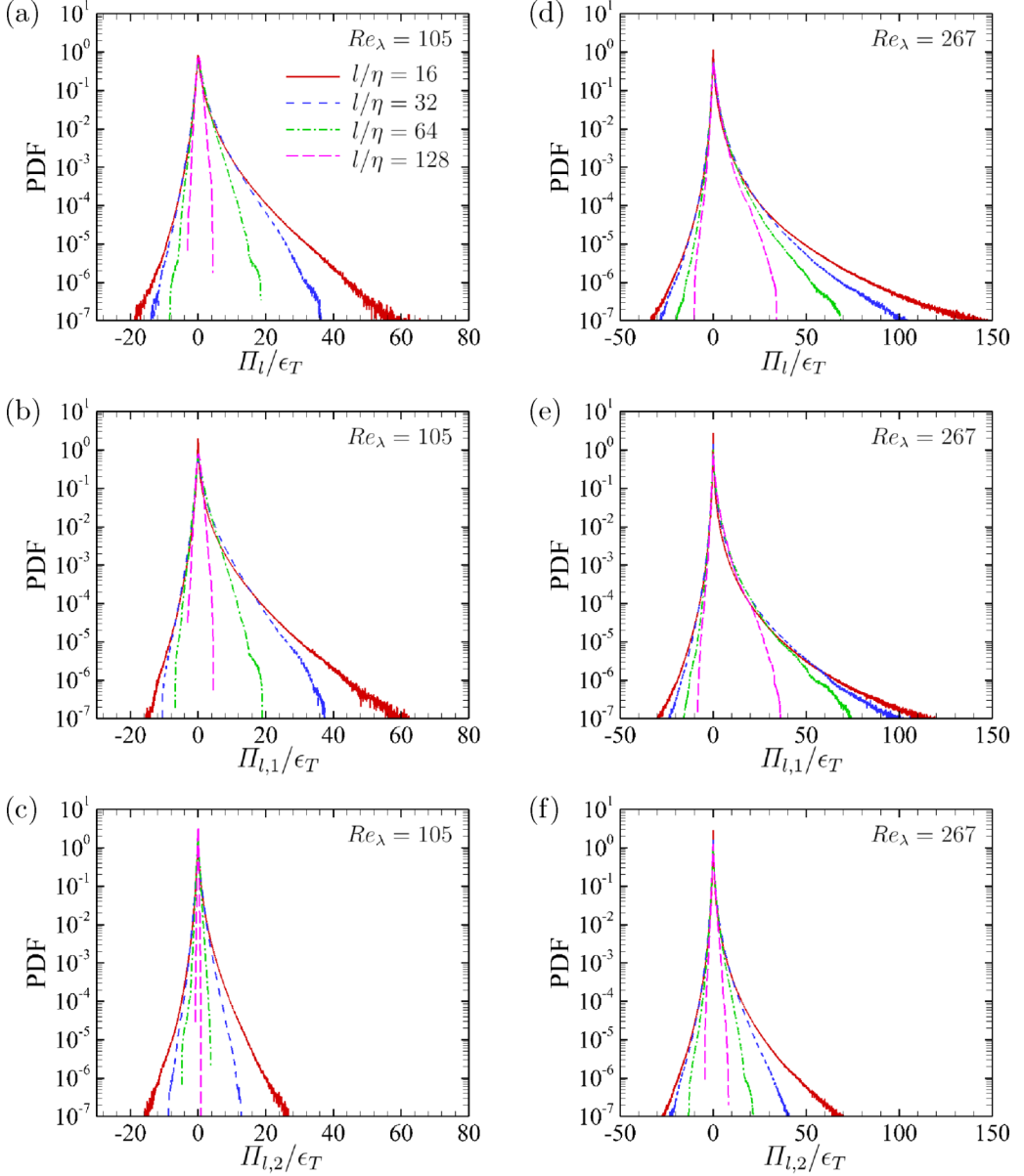
FIG. 9. PDF of the normalized SGS flux for different filter widths $l/\eta = 16, 32, 64, 128$ at $M_t = 1.0$ and at two Taylor Reynolds numbers (a)–(c) $Re_\lambda = 105$ and (d)–(f) $Re_\lambda = 267$. (a), (d) Π_l/ϵ_T; (b), (e) $\Pi_{l,1}/\epsilon_T$; (c), (f) $\Pi_{l,2}/\epsilon_T$.

5. Effect of velocity divergence on SGS flux of kinetic energy

For compressible flow, the dilatation serves as an excellent indicator of local compressibility. More insight into the effect of the compressibility on SGS flux of kinetic energy can be gained from the joint PDF of the normalized SGS kinetic energy flux and the normalized filtered velocity divergence. Wang *et al.* [9] found that as the turbulent Mach number increases, the fractions of the second and fourth quadrants of the joint PDF become larger, while the fractions of the first and third quadrants become smaller for compressible isotropic turbulence. They also showed that the
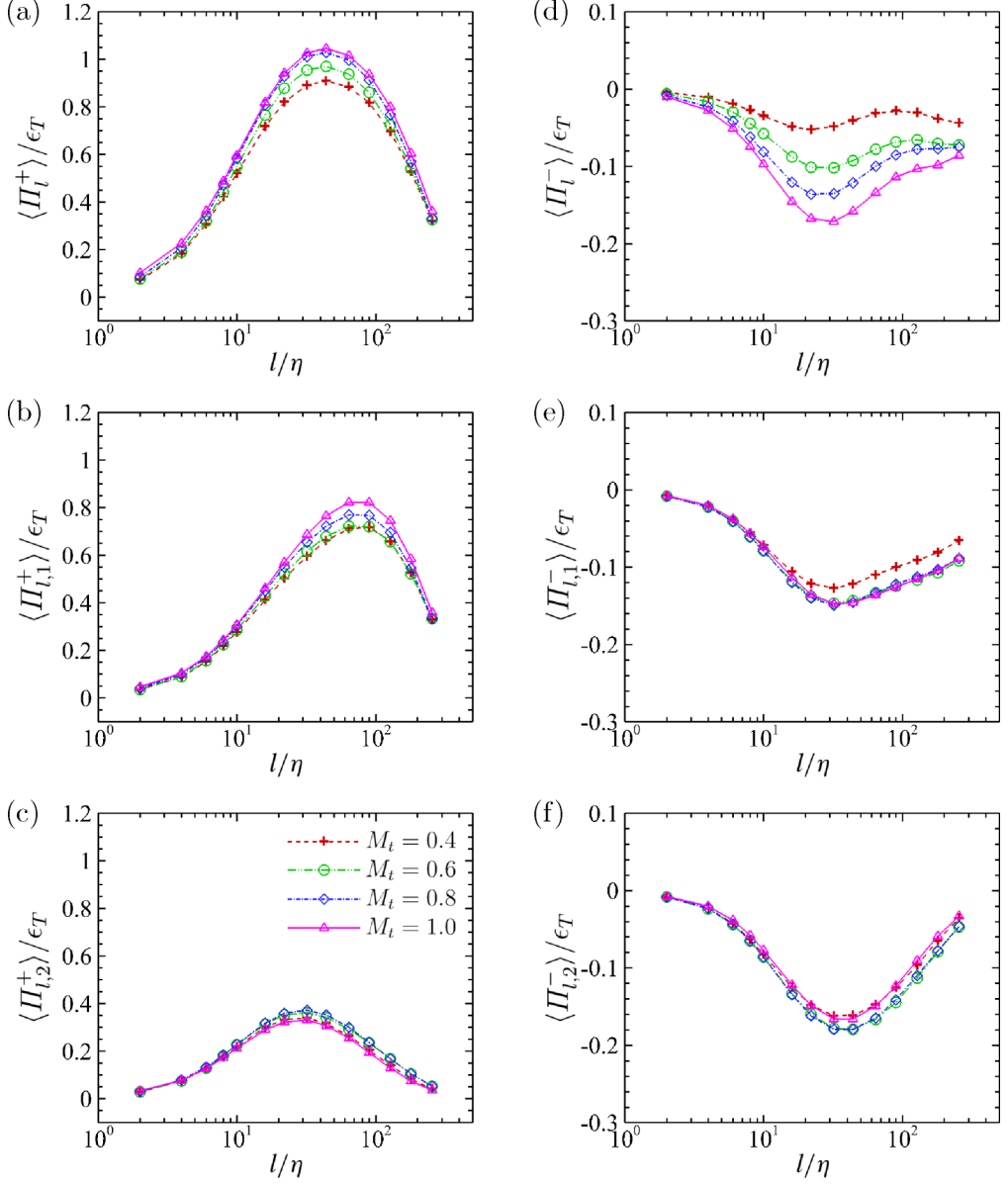
FIG. 10. Normalized average of the positive and negative components of SGS flux at different turbulent Mach numbers $M_t = 0.4, 0.6, 0.8, 1.0$ for $\mathrm{Re}_\lambda \approx 160$. (a) $\langle \Pi_l^+ \rangle / \epsilon_T$; (b) $\langle \Pi_{l,1}^+ \rangle / \epsilon_T$; (c) $\langle \Pi_{l,2}^+ \rangle / \epsilon_T$; (d) $\langle \Pi_l^- \rangle / \epsilon_T$; (e) $\langle \Pi_{l,1}^- \rangle / \epsilon_T$; (f) $\langle \Pi_{l,2}^- \rangle / \epsilon_T$.

occurrence of strong compression associated with the shocklet structure greatly enhances the direct SGS flux of kinetic energy from large scales to small scales.

The joint PDFs of $(\Pi_l/\epsilon_T, \theta_l/\theta_l')$ and $(\Pi_{l,i}/\epsilon_T, \theta_l/\theta_l')$ are shown in Fig. 12 for the case with $M_t = 1.0$ and $\mathrm{Re}_\lambda = 163$. We find that the shape of the joint PDF of $(\Pi_l/\epsilon_T, \theta_l/\theta_l')$ exhibits a strong statistical preference in the second and fourth quadrants, consistent with Wang *et al.* [9]. The shapes of the PDF$(\Pi_{l,1}/\epsilon_T, \theta_l/\theta_l')$ and PDF$(\Pi_{l,2}/\epsilon_T, \theta_l/\theta_l')$ are very similar and both become less asymmetric as compared to that of PDF$(\Pi_l/\epsilon_T, \theta_l/\theta_l')$, indicating that the filtered velocity divergence is less relevant to the SGS flux components. It is also found that the shape
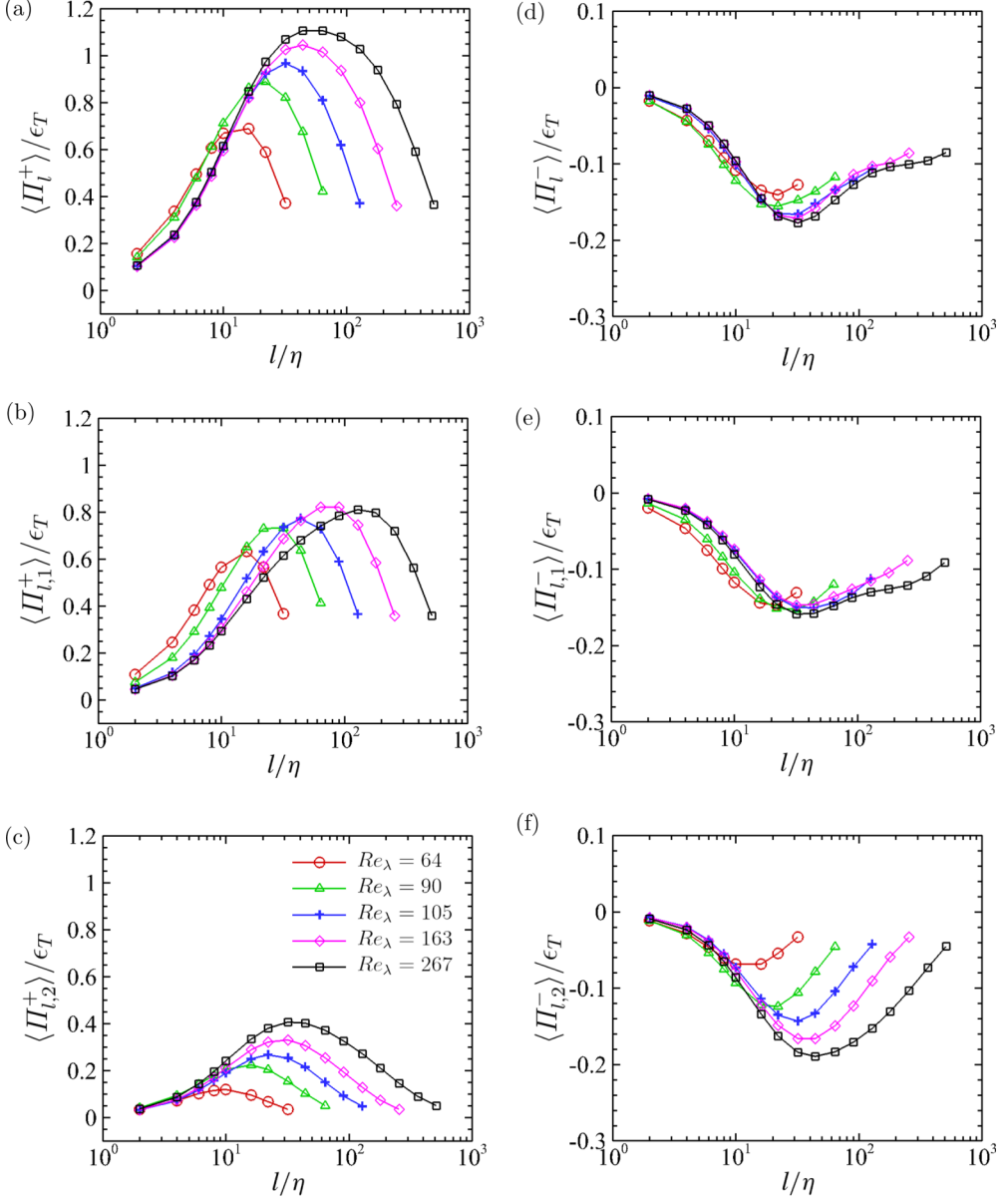
FIG. 11. Normalized average of the positive and negative components of SGS flux at different Taylor Reynolds number $Re_\lambda = 64, 90, 105, 163, 267$ for $M_t \approx 1.0$. (a) $\langle \Pi_l^+ \rangle / \epsilon_T$; (b) $\langle \Pi_{l,1}^+ \rangle / \epsilon_T$; (c) $\langle \Pi_{l,2}^+ \rangle / \epsilon_T$; (d) $\langle \Pi_l^- \rangle / \epsilon_T$; (e) $\langle \Pi_{l,1}^- \rangle / \epsilon_T$; (f) $\langle \Pi_{l,2}^- \rangle / \epsilon_T$.

of PDF($\Pi_{l,1}/\epsilon_T$, θ_l/θ_l') is slightly broader than that of PDF($\Pi_{l,2}/\epsilon_T$, θ_l/θ_l'), which is consistent with the observations in Fig. 9.

Figures 13(a)–13(c) depict the expansion regions represented by isosurfaces of the velocity divergence ($\theta_l/\theta_l' = 2$) for the filter width $l/\eta = 16$ at $M_t = 1.0$ and $Re_\lambda = 163$. The isosurfaces are colored based on the normalized SGS flux of kinetic energy. It is found that the expansion motions are bloblike and almost all of them contribute to the negative SGS flux of kinetic energy Π_l^-/ϵ_T, while the fractions of positive SGS flux components, $\Pi_{l,1}^+/\epsilon_T$ and $\Pi_{l,2}^+/\epsilon_T$, on the isosurfaces
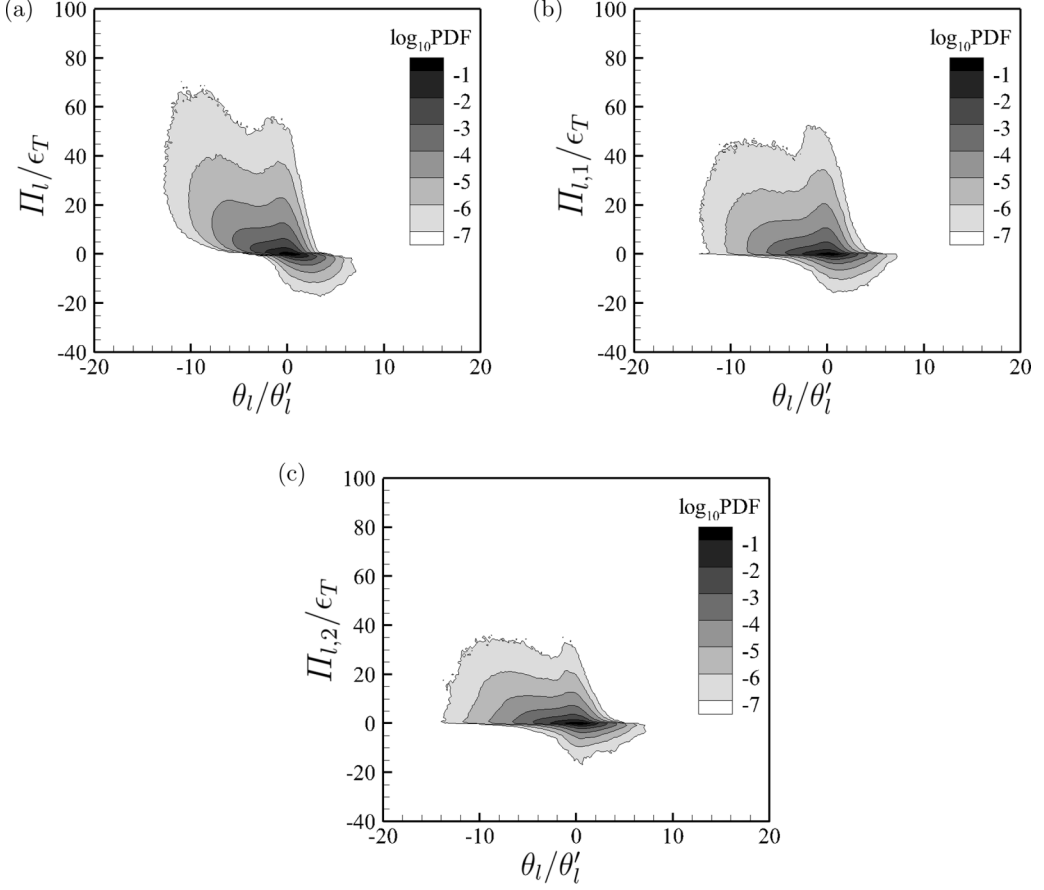
FIG. 12. Joint PDF of $\Pi_{l,i}/\epsilon_T$ and θ_l/θ_l' for the filter width $l/\eta = 16$ at $M_t = 1.0$ and $\mathrm{Re}_\lambda = 163$. (a) Π_l/ϵ_T, (b) $\Pi_{l,1}/\epsilon_T$, (c) $\Pi_{l,2}/\epsilon_T$.

increase apparently. The high compression regions are shown in Figs. 13(d)–13(f); most of them are sheetlike structures, which indicates the generation of shocklets at high turbulent Mach number $M_t = 1.0$. We find that almost all compression motions contribute to the positive SGS flux of kinetic energy Π_l^+/ϵ_T, while the fractions of negative SGS flux components, $\Pi_{l,1}^-/\epsilon_T$ and $\Pi_{l,2}^-/\epsilon_T$, on the isosurfaces increase apparently. These results imply that correlation between SGS flux components $\Pi_{l,i}/\epsilon_T$ and velocity divergence θ_l/θ_l' is weaker than that of Π_l/ϵ_T.

Figures 14(a)–14(c) show the average of normalized SGS kinetic energy flux conditioned on the normalized filtered velocity divergence θ_l/θ_l' for different filter widths $l/\eta = 16, 22, 32, 44, 64$ at $M_t = 1.0$ and $\mathrm{Re}_\lambda = 267$. We can see that both $\langle \Pi_l/\epsilon_T | \theta_l/\theta_l' \rangle$ and $\langle \Pi_{l,i}/\epsilon_T | \theta_l/\theta_l' \rangle$ are greatly dependent on filtered velocity divergence θ_l/θ_l' and nearly independent of filter width l/η for $16 \leqslant l/\eta \leqslant 64$, which is consistent with previous studies in compressible isotropic turbulence by Wang *et al.* [9]. The magnitude of $\langle \Pi_{l,1}/\epsilon_T | \theta_l/\theta_l' \rangle$ is larger than that of $\langle \Pi_{l,2}/\epsilon_T | \theta_l/\theta_l' \rangle$ in compression regions, while both are clearly smaller than that of $\langle \Pi_l/\epsilon_T | \theta_l/\theta_l' \rangle$. Wang *et al.* [9] proposed simple algebraic models for the conditionally average of SGS flux in compression regions ($\theta \leqslant 0$) and in expansion regions ($\theta \geqslant 0$), read as

$$\langle \Pi_l/\epsilon_T | \theta_l/\theta_l' \rangle = b + \alpha_0 (\theta/\theta')^n, \quad \theta \leqslant 0, \tag{34}$$

$$\langle \Pi_l/\epsilon_T | \theta_l/\theta_l' \rangle = b - \alpha_1 (\theta/\theta')^m, \quad \theta \geqslant 0, \tag{35}$$
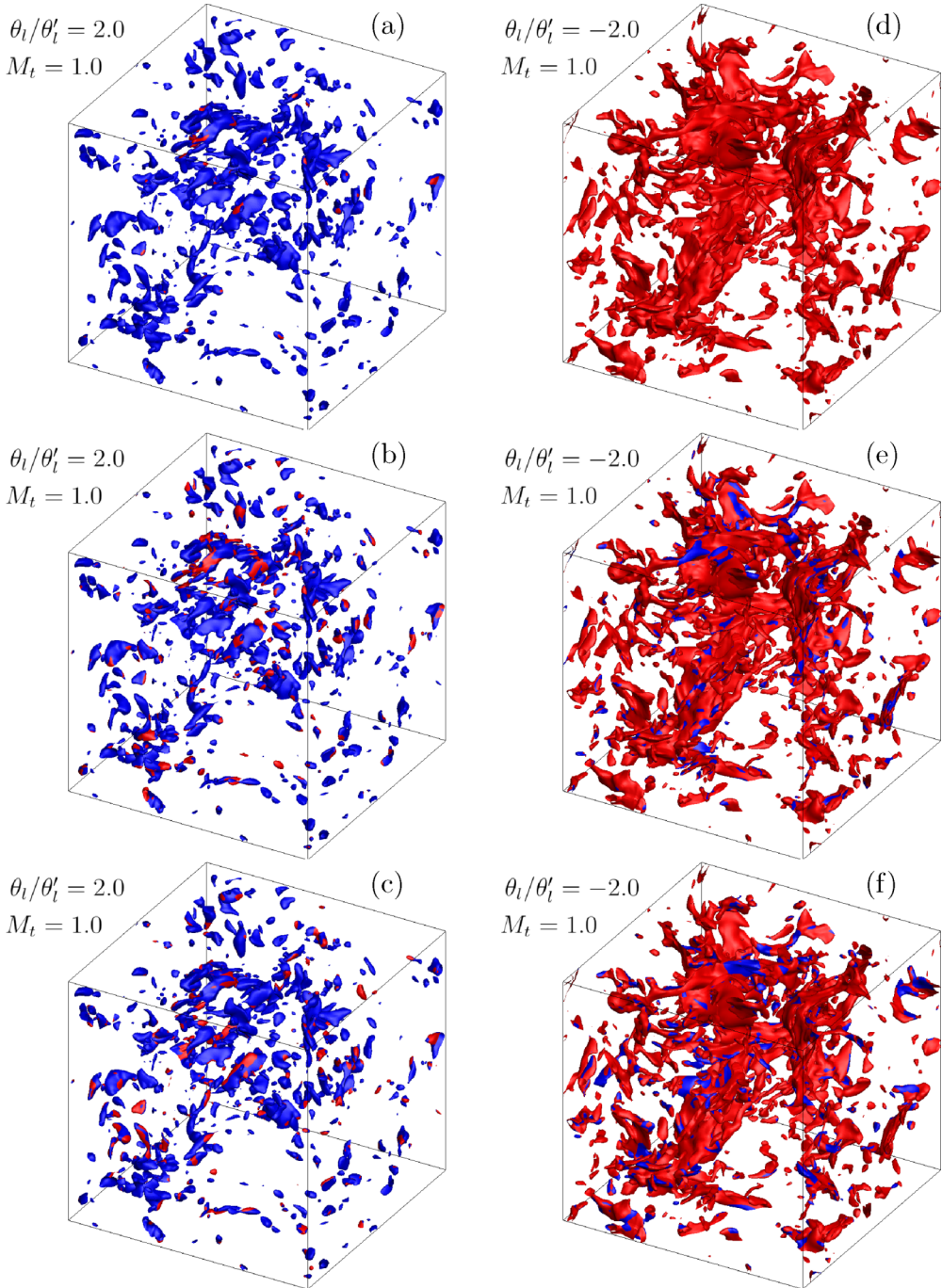
FIG. 13. Isosurfaces of (a)–(c) $\theta_l/\theta_l' = 2$ and (d)–(f) $\theta_l/\theta_l' = -2$ for the filter width $l/\eta = 16$ at $M_t = 1.0$ and $Re_\lambda = 163$. The isosurface is colored by (a), (d) Π_l/Π_l'; (b), (e) $\Pi_{l,1}/\Pi_{l,1}'$; (c), (f) $\Pi_{l,2}/\Pi_{l,2}'$. Red for positive SGS flux and blue for negative SGS flux.
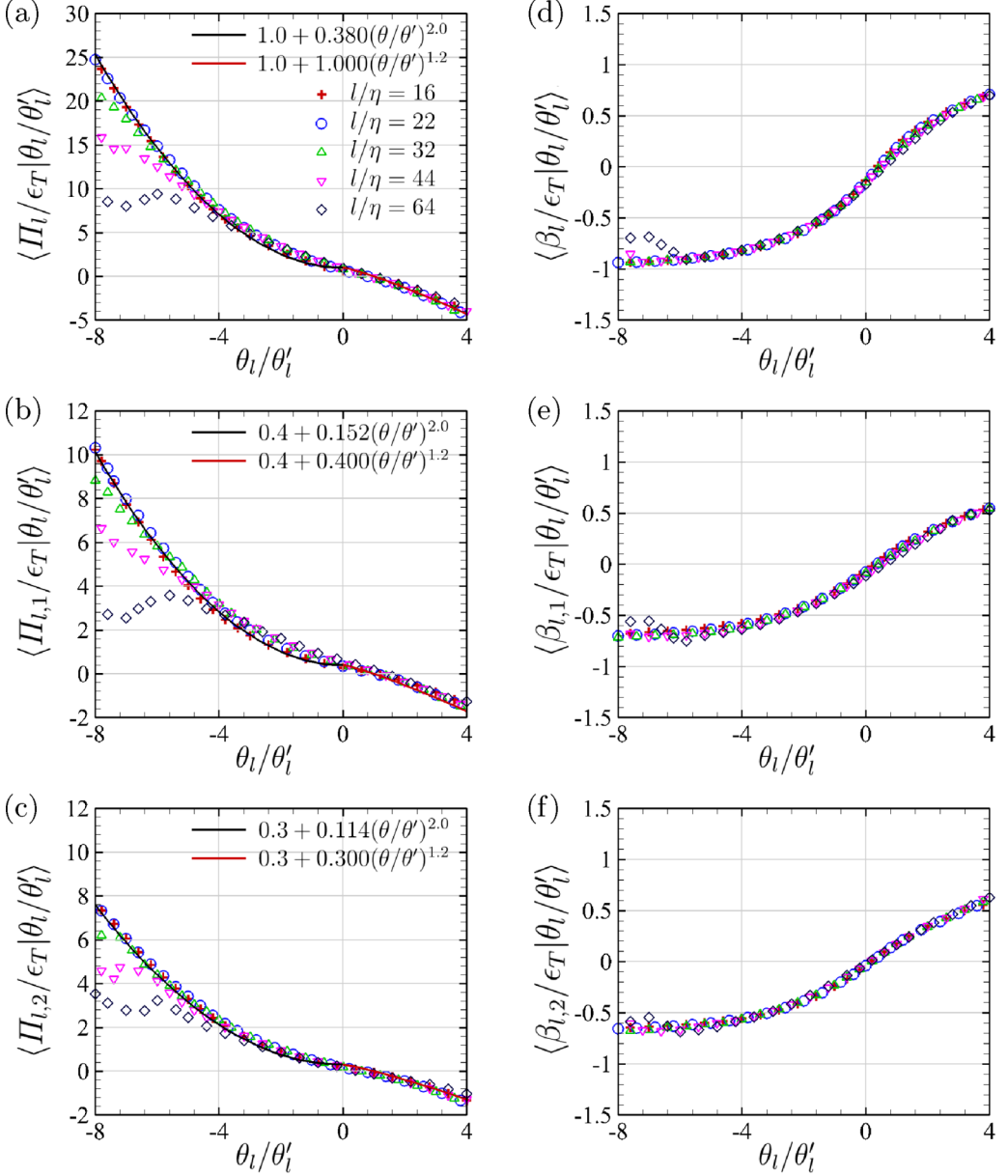
FIG. 14. Average of (a)–(c) normalized SGS flux and (d)–(f) β_l conditioned on the normalized filtered velocity divergence θ_l/θ_l' for different filter widths $l/\eta = 16, 22, 32, 44, 64$ at $M_t = 1.0$ and $\mathrm{Re}_\lambda = 267$. (a) $\langle \Pi_l/\epsilon_T|\theta_l/\theta_l'\rangle$, (b) $\langle \Pi_{l,1}/\epsilon_T|\theta_l/\theta_l'\rangle$, (c) $\langle \Pi_{l,2}/\epsilon_T|\theta_l/\theta_l'\rangle$, (d) $\langle \beta_l|\theta_l/\theta_l'\rangle$, (e) $\langle \beta_{l,1}|\theta_l/\theta_l'\rangle$, (f) $\langle \beta_{l,2}|\theta_l/\theta_l'\rangle$.

where $b = 1$, $\alpha_0 = 0.42$, $\alpha_1 = 1.0$, $n = 2.0$, and $m = 1.2$ at $M_t = 1.0$ and $\mathrm{Re}_\lambda \approx 260$ in compressible isotropic turbulence. The intercept b is the normalized SGS flux in incompressible flow and tends to 1 in the inertial range at high Taylor Reynolds numbers. For isotropic turbulence, $\langle \Pi_{l,i}/\epsilon_T|\theta_l/\theta_l'\rangle = 1/3\langle \Pi_l/\epsilon_T|\theta_l/\theta_l'\rangle$ exactly. For FAT at $M_t = 1.0$ and $\mathrm{Re}_\lambda = 267$, it is found that $\alpha_0 = 0.38$ is a little smaller than 0.42 in isotropic turbulence, and $\langle \Pi_{l,1}/\epsilon_T|\theta_l/\theta_l'\rangle = 0.4\langle \Pi_l/\epsilon_T|\theta_l/\theta_l'\rangle$, $\langle \Pi_{l,2}/\epsilon_T|\theta_l/\theta_l'\rangle = 0.3\langle \Pi_l/\epsilon_T|\theta_l/\theta_l'\rangle$, as indicated by solid lines in Figs. 14(a)–14(c).

The anisotropy of the conditional average of SGS flux can be interpreted by the relation between the large-scale strain and the SGS stress which is denoted by β_l, defined as

$$\beta_l \equiv (\widetilde{\tau}_{ij}\widetilde{S}_{ij})/(|\widetilde{\tau}||\widetilde{\mathbf{S}}|), \tag{36}$$

where $|\widetilde{\tau}| = \sqrt{\widetilde{\tau}_{ij}\widetilde{\tau}_{ij}}$ and $|\widetilde{\mathbf{S}}| = \sqrt{\widetilde{S}_{ij}\widetilde{S}_{ij}}$. The three components $\beta_{l,i}$ can be obtained by avoiding summation convention over repeated index i in Eq. (36). The average of β_l conditioned on the normalized filtered velocity divergence θ_l/θ_l' for different filter widths $l/\eta = 16, 22, 32, 44, 64$ at $M_t = 1.0$ and $\mathrm{Re}_\lambda = 267$ is shown in Figs. 14(d)–14(f). We find that $\langle \beta_l | \theta_l/\theta_l' \rangle$ is close to -1 when $\theta_l/\theta_l' < -5$, indicating the antiparallel alignment between the large-scale strain and the SGS stress. The conditional averages of $\beta_{l,1}$ and $\beta_{l,2}$ approach -0.7 and -0.6, respectively, for $\theta_l/\theta_l' < -5$. The nonparallel alignment between the large-scale strain and SGS stress decreases the efficiency of interscale kinetic energy transfer in the streamwise and transverse directions.

6. Kinetic energy transfer in spectral space

In this section we present kinetic energy transfers in spectral space and make a rudimentary comparison with that in physical space. In spectral space, the kinetic energy equation is derived by multiplying the Fourier representation of the governing equation for density-weighted variable $\mathbf{w} = \sqrt{\rho}\mathbf{u}$ by its complex conjugate $\hat{\mathbf{w}}^*$ [15,51,52], and integrating inside the sphere of radius $k = |\mathbf{k}|$ to obtain

$$\frac{\partial}{\partial t}\hat{E}_k = -\hat{\Pi}_k - \hat{\Phi}_k - \hat{D}_k + \hat{P}_k, \tag{37}$$

where $\hat{E}_k$ is total kinetic energy inside the sphere of radius k. $\hat{\Pi}_k$ is the kinetic energy transfer between the lower wave numbers inside and the higher wave numbers outside the sphere of radius k, namely, between large scales and small scales. $\hat{\Phi}_k$ and $\hat{D}_k$ are the total pressure dilatation and the total viscous dissipation rate inside the sphere, respectively. The last term $\hat{P}_k$ is the total energy injection rate inside the sphere by the external force. These terms are defined as

$$\hat{E}_k = \sum_{|\mathbf{k}|<k} \frac{1}{2}\hat{w}_i(\mathbf{k})\hat{w}_i^*(\mathbf{k}), \tag{38}$$

$$\hat{\Pi}_k = -\sum_{|\mathbf{k}|<k} \mathfrak{Im}\left[\sum_{\mathbf{m}+\mathbf{n}=\mathbf{k}} \left(k_j\hat{u}_j(\mathbf{m})\hat{w}_i(\mathbf{n})\hat{w}_i^*(\mathbf{k}) + \frac{1}{2}k_j\hat{w}_i(\mathbf{m})\hat{u}_j(\mathbf{n})\hat{w}_i^*(\mathbf{k})\right)\right], \tag{39}$$

$$\hat{\Phi}_k = -\sum_{|\mathbf{k}|<k} \mathfrak{Im}\left[\sum_{\mathbf{m}+\mathbf{n}=\mathbf{k}} k_i\hat{a}(\mathbf{m})\hat{p}(\mathbf{n})\hat{w}_i^*(\mathbf{k})\right], \tag{40}$$

$$\hat{D}_k = \frac{1}{\mathrm{Re}}\sum_{|\mathbf{k}|<k} \mathfrak{Im}\left[\sum_{\mathbf{m}+\mathbf{n}=\mathbf{k}} k_j\hat{a}(\mathbf{m})\hat{b}_{ij}(\mathbf{n})\hat{w}_i^*(\mathbf{k})\right], \tag{41}$$

$$\hat{P}_k = \sum_{|\mathbf{k}|<k} \mathfrak{Re}[\hat{F}_i(\mathbf{k})\hat{w}_i^*(\mathbf{k})], \tag{42}$$

where $\hat{a} = \mathcal{F}_k\{\rho^{-1/2}\}$, $\hat{b}_{ij} = \mathcal{F}_k\{\sigma_{ij}\}$, and $\mathcal{F}_k\{\cdot\}$ indicates the Fourier transform of the argument in curly brackets; $\mathfrak{Re}[\cdot]$ and $\mathfrak{Im}[\cdot]$ represent the real and imaginary components of the argument in square brackets, respectively. It is straightforward to obtain the equations for three components of kinetic energy in spectral space by avoiding the summation convention over repeated index i in the above equations. This yields

$$\frac{\partial}{\partial t}\hat{E}_{k,i} = -\hat{\Pi}_{k,i} - \hat{\Phi}_{k,i} - \hat{D}_{k,i} + \hat{P}_{k,i}. \tag{43}$$
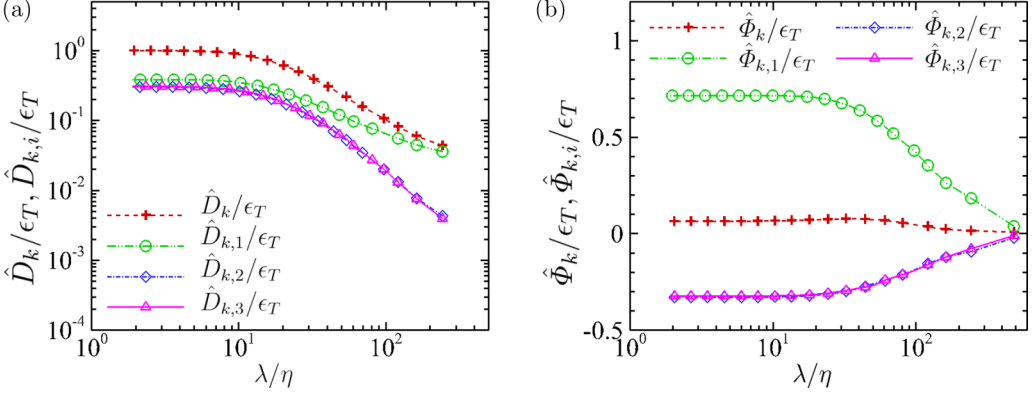
FIG. 15. Normalized (a) viscous dissipation and (b) pressure-strain terms in spectral space at $\mathrm{Re}_\lambda = 163$ and $M_t = 1.0$.

We can find that Eqs. (37) and (43) are similar to Eqs. (16) and (24) for the kinetic energy in physical space.

We plot the normalized viscous dissipation and pressure-strain terms in the spectral transport equations (37) and (43) at $\mathrm{Re}_\lambda = 163$ and $M_t = 1.0$ in Fig. 15, and they are shown as functions of wavelength $\lambda = 2\pi/k$ for the convenience of comparison. It is found that the normalized viscous dissipation and pressure-strain terms are very similar to those in physical space, as shown in Figs. 2 and 4. In spectral space, the observed decrease of the viscous dissipation term starts to appear at length scale $\lambda/\eta \approx 10$, and at $\lambda/\eta \approx 20$ for the pressure-strain term, while both start to decrease at smaller length scale in physical space. It is also found that the viscous dissipation term presents a slower decay than that in physical space at large scales. As expected, these two terms are insensitive to the change of turbulent Mach number in our simulations, and the results for other turbulent Mach number are omitted here for brevity.

In Figs. 16(a) and 16(b), we depict the normalized energy flux in spectral space at $M_t = 0.4$, 1.0 and $\mathrm{Re}_\lambda \approx 160$. The normalized total energy flux $\hat{\Pi}_k/\epsilon_T$ at $M_t = 0.4$ is consistent with previous numerical results in incompressible turbulent flow [53,54]. We find that the anisotropic property in both real and spectral space is quite similar at $\lambda/\eta > 10$. Both $\hat{\Pi}_k/\epsilon_T$ and $\hat{\Pi}_{k,i}/\epsilon_T$ are obviously small at scales $\lambda/\eta < 10$, especially for small turbulent Mach number $M_t = 0.4$, which agrees with the results by using the sharp spectral filter [9]. In contrast to the behavior of the three components of energy flux in physical space, $\hat{\Pi}_{k,2}/\epsilon_T$ and $\hat{\Pi}_{k,3}/\epsilon_T$ are larger than $\hat{\Pi}_{k,1}/\epsilon_T$ at small scales $\lambda/\eta < 10$ and high turbulent Mach number $M_t = 1.0$. In analogy with the analysis in physical space, we decompose the energy fluxes into positive and negative parts, as shown in Fig. 16(c). At small scales $\lambda/\eta < 10$, the magnitudes of $\hat{\Pi}_k^+/\epsilon_T$, $\hat{\Pi}_{k,i}^+/\epsilon_T$ and $\hat{\Pi}_k^-/\epsilon_T$, $\hat{\Pi}_{k,i}^-/\epsilon_T$ are nearly equal to each other and are much larger than 1, which is consistent with the previous study by Wang et al. [9] in compressible isotropic turbulence and by Lee et al. [55] in incompressible turbulence. It is known that the sharp spectral truncation of density can have negative values in physical space, which would violate fundamental conservation laws [14]. The numerical results of Wang et al. [9] show that, in compressible turbulence, the statistics of the energy flux of kinetic energy in physical space by the sharp spectral filter are obviously different from those by the top-hat filter and the Gaussian filter. Thus, the sharp spectral truncation is rarely applied in the study of compressible turbulence.

B. Homogeneous shear turbulence

The natural energy-generation mechanism of any shear flows is that the production term draws energy from the mean flow, the largest-scale fluid motion, and deposits it into the fluctuating field, which is fully retained within HST. The production term $-S\langle\overline{\rho}\widetilde{u_1}\widetilde{u_2}\rangle$ and overall kinetic energy
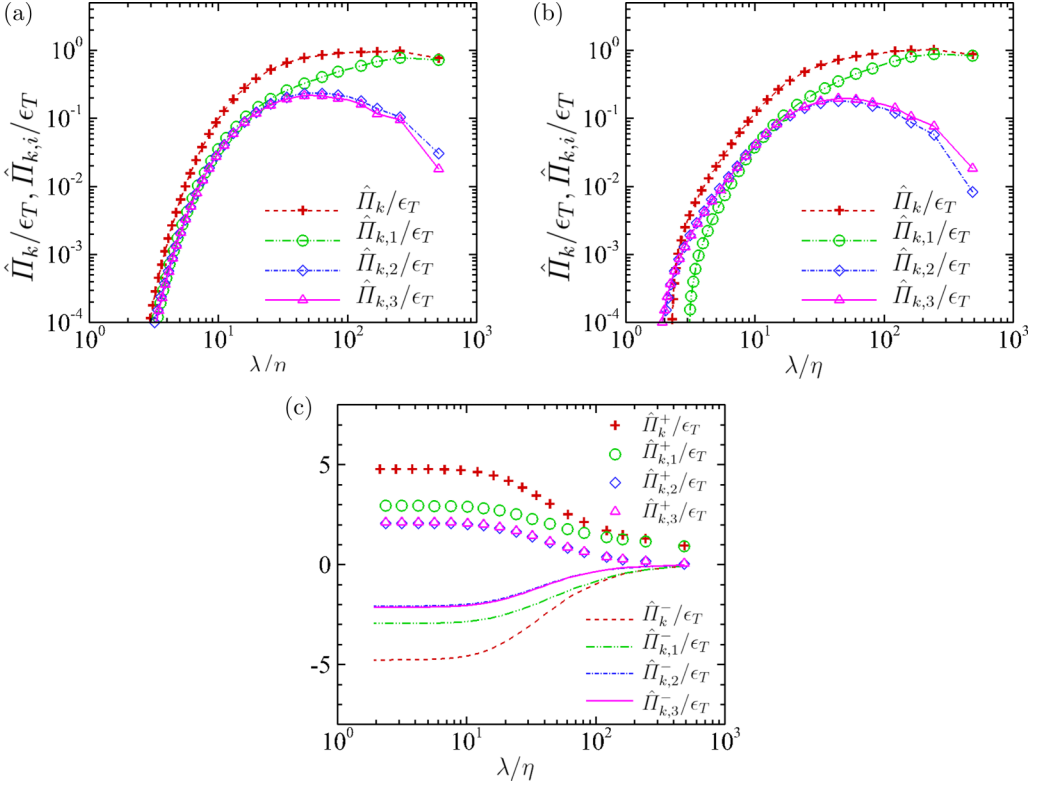
FIG. 16. Normalized energy flux in spectral space at (a) Re_λ=156, M_t=0.4 and (b) Re_λ=163, $M_t = 1.0$. (c) The normalized positive and negative components of energy flux in spectral space at $Re_\lambda = 163$, $M_t = 1.0$.

transfer for HST are shown in Fig. 17(a) at $Re_\lambda = 156$ and $M_t = 0.46$. Since the kinetic energy is all fed into the streamwise component, the production term is precisely balanced by the overall kinetic energy transfer. It is worth noting that the effect of the production term is similar to that of
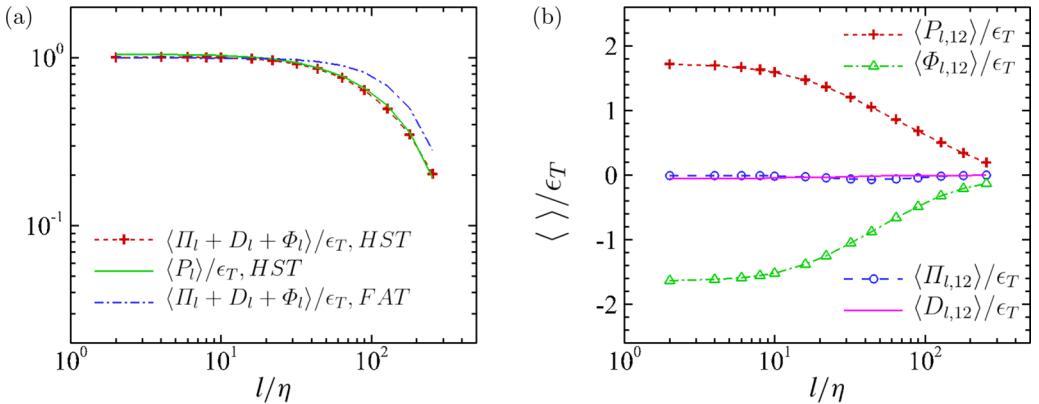
FIG. 17. Average production term $-S\langle\overline{\rho}\widetilde{u_1}\widetilde{u_2}\rangle$ and overall kinetic energy transfer for HST at $Re_\lambda = 156$ and $M_t = 0.46$, compared to overall kinetic energy transfer for FAT at $Re_\lambda = 156$ and $M_t = 0.40$. (b) Average of transfer terms of large scale Reynolds shear stress at $Re_\lambda = 156$ and $M_t = 0.46$.
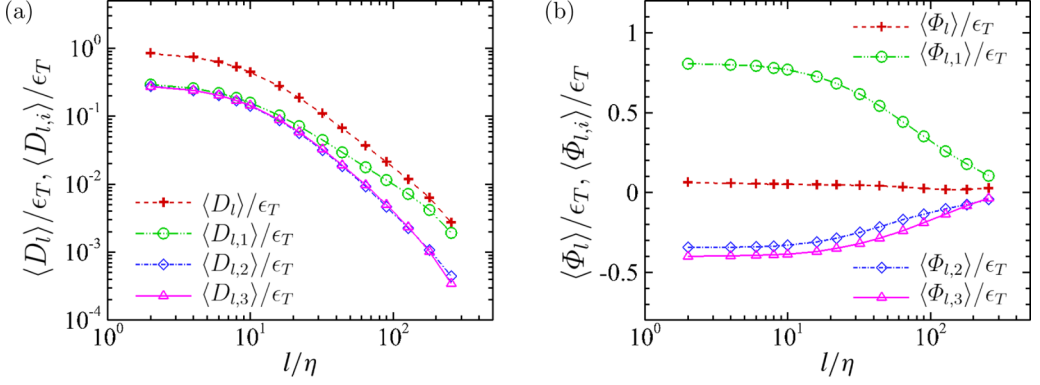
FIG. 18. Average of (a) viscous dissipation terms $\langle D_l \rangle / \epsilon_T$, $\langle D_{l,i} \rangle / \epsilon_T$, and (b) pressure-strain terms $\langle \Phi_l \rangle / \epsilon_T$, $\langle \Phi_{l,i} \rangle / \epsilon_T$ at $\mathrm{Re}_\lambda = 156$ and $M_t = 0.46$.

large-scale external forcing in FAT, i.e., kinetic energy is generated mainly at large scales, while the effect extends to much smaller scale $l/\eta \approx 50$ as compared with FAT at $\mathrm{Re}_\lambda \approx 160$ [see Fig. 1(b)].

One of the major differences between FAT and HST is the significant Reynolds shear stress in HST. Average values of transfer terms of large-scale Reynolds shear stress $\langle \overline{\rho} \widetilde{u_1} \widetilde{u_2} \rangle$ are shown
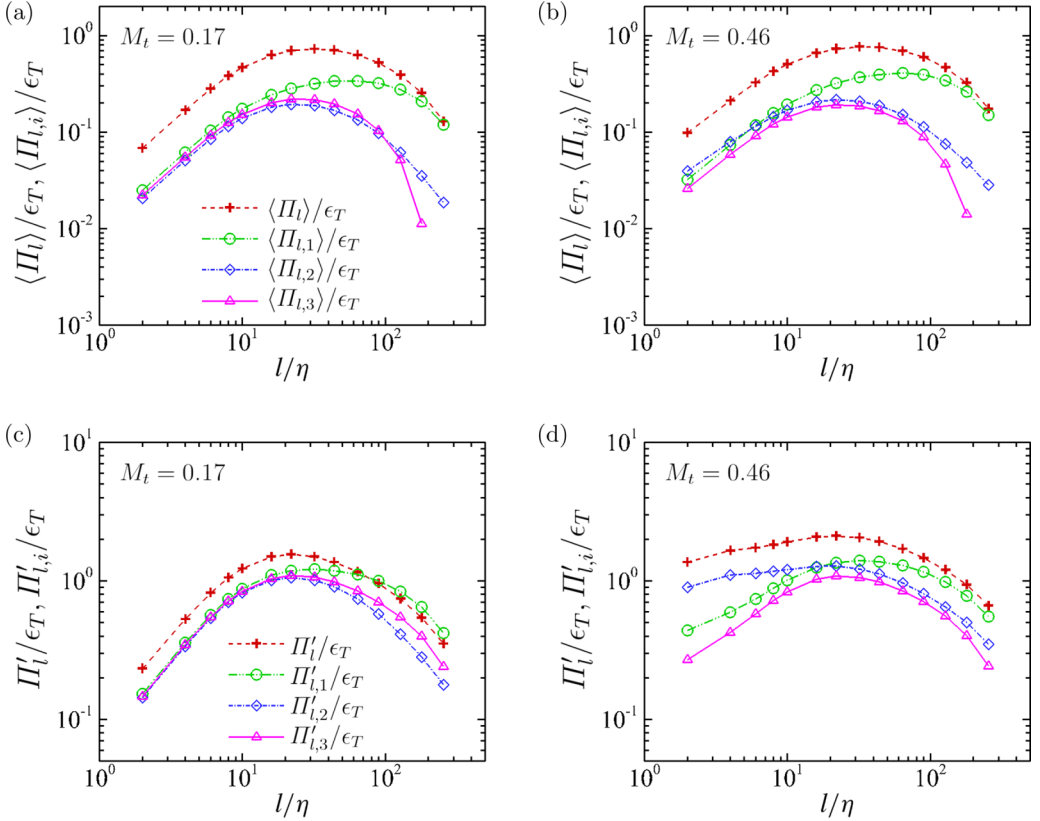
FIG. 19. (a), (b) Average of SGS flux $\langle \Pi_l \rangle / \epsilon_T$ and $\langle \Pi_{l,i} \rangle / \epsilon_T$; (c), (b) rms values of SGS flux Π'_l / ϵ_T and $\Pi'_{l,i} / \epsilon_T$ for HST. (a), (c) $\mathrm{Re}_\lambda = 145$ and $M_t = 0.17$; (b), (d) $\mathrm{Re}_\lambda = 156$ and $M_t = 0.46$.
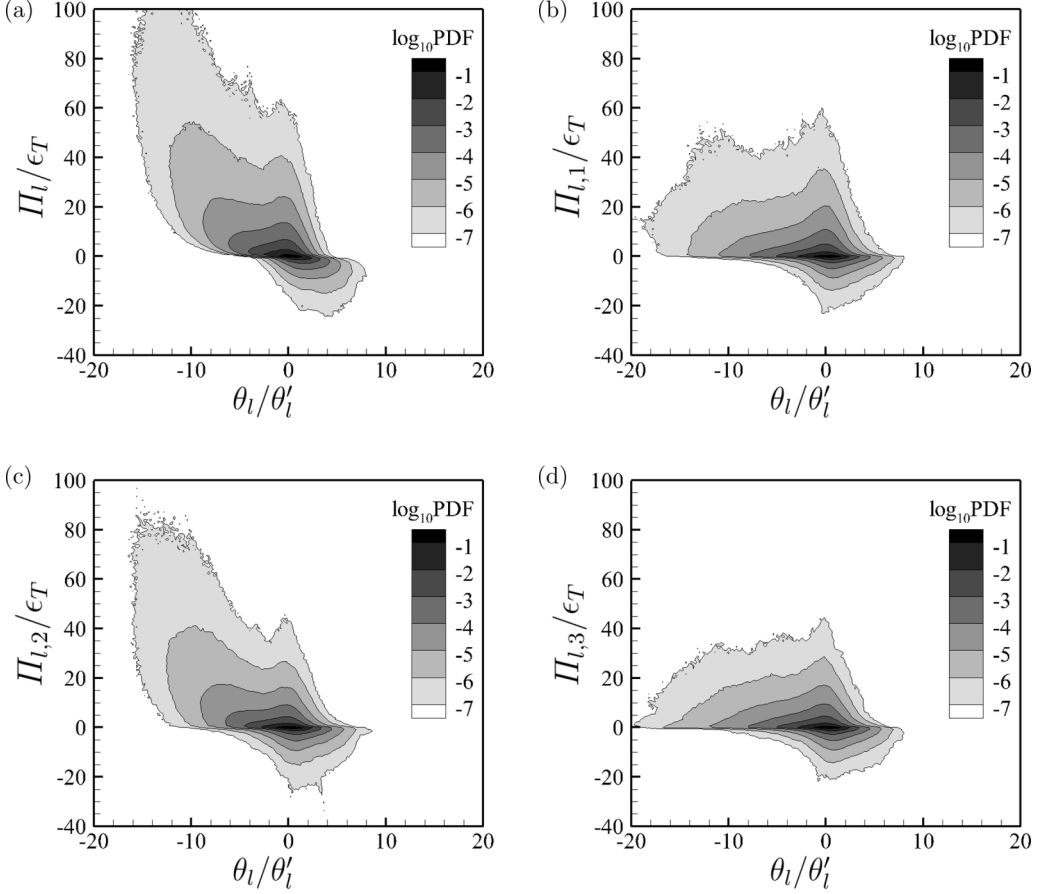
FIG. 20. Joint PDF of $\Pi_{l,i}/\epsilon_T$ and θ_l/θ_l' for the filter width $l/\eta = 16$ at turbulent Mach number $M_t = 0.46$. (a) Π_l/ϵ_T, (b) $\Pi_{l,1}/\epsilon_T$, (c) $\Pi_{l,2}/\epsilon_T$, (d) $\Pi_{l,3}/\epsilon_T$.

in Fig. 17(b) at $Re_\lambda = 156$ and $M_t = 0.46$. We can see that the transfer of large-scale Reynolds shear stress $\langle \overline{\rho} \widetilde{u}_1 \widetilde{u}_2 \rangle$ is dominated by the pressure-strain term $2\langle \overline{p} \widetilde{S}_{12} \rangle$ and production term $-\langle \overline{\rho} \widetilde{u}_2^2 \rangle$, while the viscous dissipation and SGS flux are negligibly small. The magnitudes of $2\langle \overline{p} \widetilde{S}_{12} \rangle$ and $-\langle \overline{\rho} \widetilde{u}_2^2 \rangle$ are 1.5 times larger than total dissipation of kinetic energy ϵ_T at small filter width $l/\eta \approx 10$. This observation is consistent with a previous numerical study of kinetic energy transfer in weak compressible HST by Hamba [56]. In Fig. 18, we plot averages of viscous dissipation and pressure-strain terms of large-scale kinetic energy for HST at $Re_\lambda = 156$ and $M_t = 0.46$. The viscous dissipation term is similar to that in FAT [see Fig. 2(a)]. The pressure-strain terms $\langle \Phi_{l,2} \rangle$ and $\langle \Phi_{l,3} \rangle$ are clearly unequal, indicating that the energies redistributed from $\langle \frac{1}{2} \overline{\rho} \widetilde{u}_1 \widetilde{u}_1 \rangle$ to $\langle \frac{1}{2} \overline{\rho} \widetilde{u}_2 \widetilde{u}_2 \rangle$ and $\langle \frac{1}{2} \overline{\rho} \widetilde{u}_3 \widetilde{u}_3 \rangle$ are different.

In Fig. 19, we plot the average of SGS kinetic energy flux for HST at $M_t = 0.17$ and 0.46. As expected, the SGS kinetic energy flux is dominated by the streamwise component at large scales in homogeneous shear turbulence. At a higher turbulent Mach number $M_t = 0.46$, the vertical SGS kinetic energy flux component $\langle \Pi_{l,2} \rangle$ is larger than the streamwise component $\langle \Pi_{l,1} \rangle$ at small scales. This high-level anisotropy at the high turbulent Mach number can be more clearly observed from the rms values of SGS kinetic energy flux, as shown in Fig. 19(d).

We focus on the effect of compressibility on SGS kinetic energy flux of HST. The joint PDFs of $(\Pi_l/\epsilon_T, \theta_l/\theta_l')$ and $(\Pi_{l,i}/\epsilon_T, \theta_l/\theta_l')$ are shown in Fig. 20 for $M_t = 0.46$ and $Re_\lambda = 156$. The
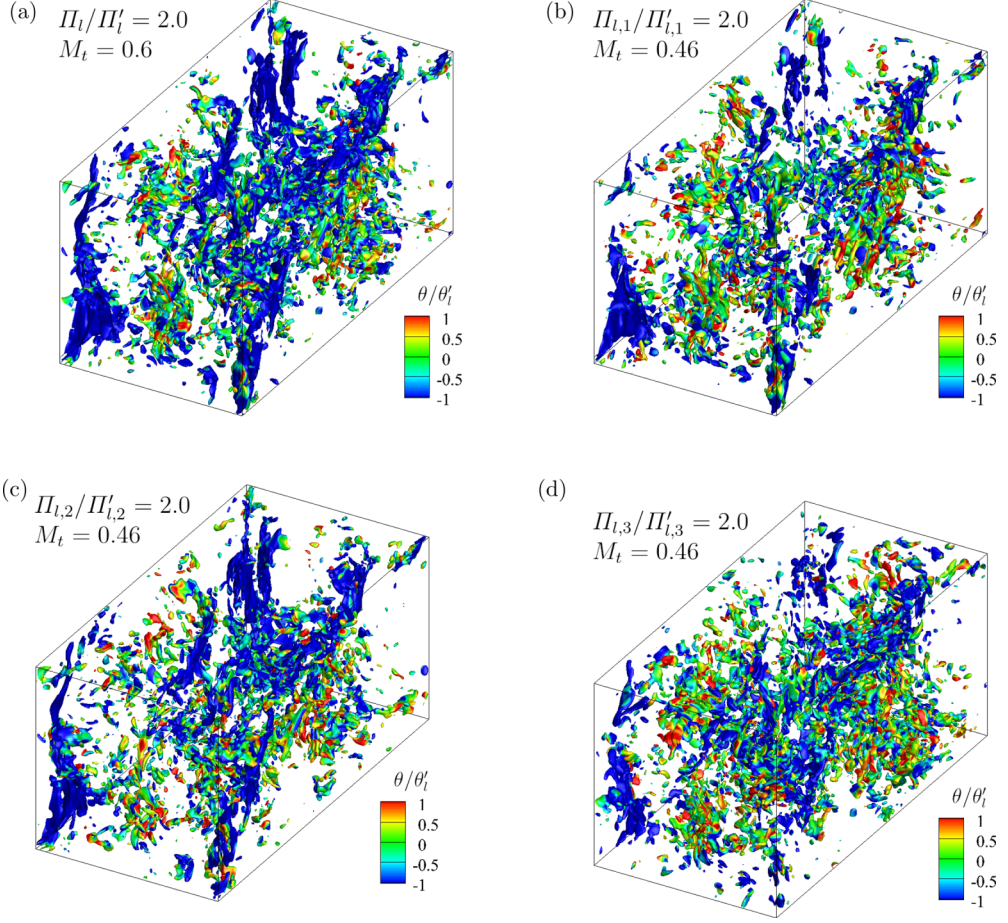
FIG. 21. Isosurfaces of normalized SGS flux at $\Pi_l/\Pi_l' = 2.0$ and $\Pi_{l,i}/\Pi_{l,i}' = 2.0$ for the filter width $l/\eta = 16$ at $M_t = 0.46$. (a) Π_l/Π_l'; (b) $\Pi_{l,1}/\Pi_{l,1}'$; (c) $\Pi_{l,2}/\Pi_{l,2}'$; (d) $\Pi_{l,3}/\Pi_{l,3}'$.

fractions of the second quadrant of the joint PDF of (Π_l/ϵ_T, θ_l/θ_l') are much larger as compared to that for FAT at $M_t = 1.0$ and $\mathrm{Re}_\lambda = 163$ [shown in Fig. 12(a)], indicating that the effect of compressibility is more prominent in HST [45,57]. It is interesting to observe that the shape of the joint PDF of ($\Pi_{l,2}/\epsilon_T$, θ_l/θ_l') is much more asymmetric than those of $\Pi_{l,1}/\epsilon_T$ and $\Pi_{l,3}/\epsilon_T$. Therefore, in HST, strong compression motions induce strong direct SGS flux of vertical kinetic energy $\Pi_{l,2}/\epsilon_T$, possibly explaining the larger $\Pi_{l,2}$ at small scales at turbulent Mach number $M_t = 0.46$, as shown in Fig. 19(b).

Figure 21 depicts the isosurfaces of normalized SGS kinetic energy flux at $\Pi_l/\Pi_l' = 2$ and $\Pi_{l,i}/\Pi_{l,i}' = 2$ for the filter width $l/\eta = 16$, at turbulent Mach number $M_t = 0.46$. The isosurfaces are colored based on the normalized filtered velocity divergence θ_l/θ_l'. The isosurfaces of $\Pi_l/\Pi_l' = 2$ are the mixture of sheetlike and bloblike structures. The sheetlike structures are associated with strong compression motions and exhibit much larger length scales than the bloblike structures, indicating the generations of shocklets at higher turbulent Mach number $M_t = 0.46$ [45]. The strong compression motions mainly contribute to the positive SGS flux of kinetic energy. The large-scale sheetlike structures of the isosurface of $\Pi_{l,2}/\Pi_{l,2}' = 2$ are similar to that of $\Pi_l/\Pi_l' = 2$, while those of $\Pi_{l,1}/\Pi_{l,1}' = 2$ and $\Pi_{l,3}/\Pi_{l,3}' = 2$ evidently decrease, demonstrating that the effect of compressibility on $\Pi_{l,2}$ is much stronger than that on $\Pi_{l,1}$ and $\Pi_{l,3}$.
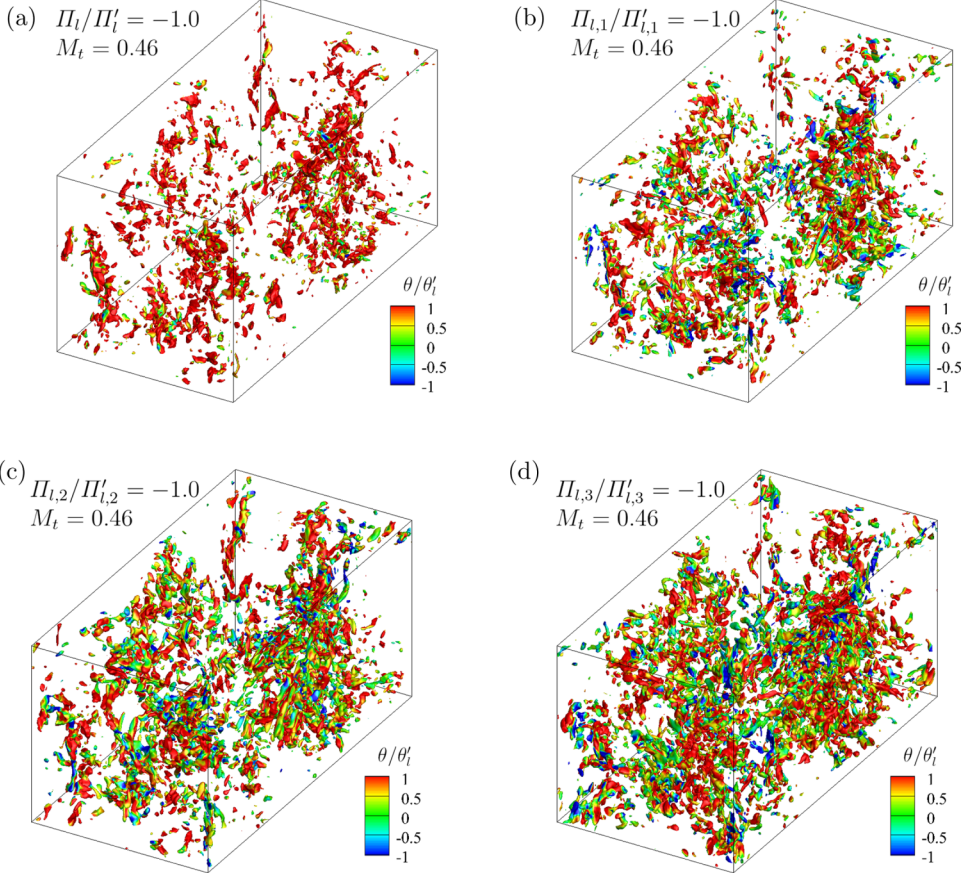
FIG. 22. Isosurfaces of normalized SGS flux at $\Pi_l/\Pi_l' = -1.0$ and $\Pi_{l,i}/\Pi_{l,i}' = -1.0$ for the filter width $l/\eta = 16$ at $M_t = 0.46$. (a) Π_l/Π_l'; (b) $\Pi_{l,1}/\Pi_{l,1}'$; (c) $\Pi_{l,2}/\Pi_{l,2}'$; (d) $\Pi_{l,3}/\Pi_{l,3}'$.

The isosurfaces of normalized SGS kinetic energy flux at $\Pi_l/\Pi_l' = -1.0$ and $\Pi_{l,i}/\Pi_{l,i}' = -1.0$ for the filter width $l/\eta = 16$ at turbulent Mach number $M_t = 0.46$ are shown in Fig. 22. The isosurfaces are colored based on the normalized filtered velocity divergence θ_l/θ_l'. Intuitively, the isosurfaces of $\Pi_l/\Pi_l' = -1.0$ and $\Pi_{l,i}/\Pi_{l,i}' = -1.0$ are mainly bloblike structures and uniformly distributed over the whole flow field, as compared with the isosurfaces of positive SGS flux. The bloblike structures of $\Pi_l/\Pi_l' = -1.0$ are more sparse than that of $\Pi_{l,i}/\Pi_{l,i}' = -1.0$. Most of isosurfaces $\Pi_l/\Pi_l' = -1.0$ are distributed in strong expansion regions $\theta_l/\theta_l' > 1.0$, while the isosurfaces $\Pi_{l,i}/\Pi_{l,i}' = -1.0$ are nearly equally distributed in compression regions and expansion regions.

To obtain a more quantitative picture of the effect of compressibility on SGS flux of kinetic energy, the average of normalized SGS flux conditioned on the normalized filtered velocity divergence θ_l/θ_l' is shown for different filter widths $l/\eta = 16, 22, 32, 44, 64$ at $M_t = 0.46$ and $\mathrm{Re}_\lambda = 156$ in Fig. 23. The SGS kinetic energy flux of HST exhibits the scale-invariant property, which is consistent with that observed in FAT shown in Fig. 14 and in isotropic turbulence by Wang *et al.* [9]. It is found that in high compression region $\theta_l/\theta_l' > 4$, the conditional averages of three SGS flux components satisfy the relationship $\langle \Pi_{l,3}/\epsilon_T | \theta_l/\theta_l' \rangle < \langle \Pi_{l,1}/\epsilon_T | \theta_l/\theta_l' \rangle < \langle \Pi_{l,2}/\epsilon_T | \theta_l/\theta_l' \rangle$, which indicates that the local SGS kinetic energy transfer of $\langle \frac{1}{2}\overline{\rho}\widetilde{u}_2^2 \rangle$ is affected more significantly by strong compression motions, as compared to $\langle \frac{1}{2}\overline{\rho}\widetilde{u}_1^2 \rangle$ and $\langle \frac{1}{2}\overline{\rho}\widetilde{u}_3^2 \rangle$. For HST, similar algebraic
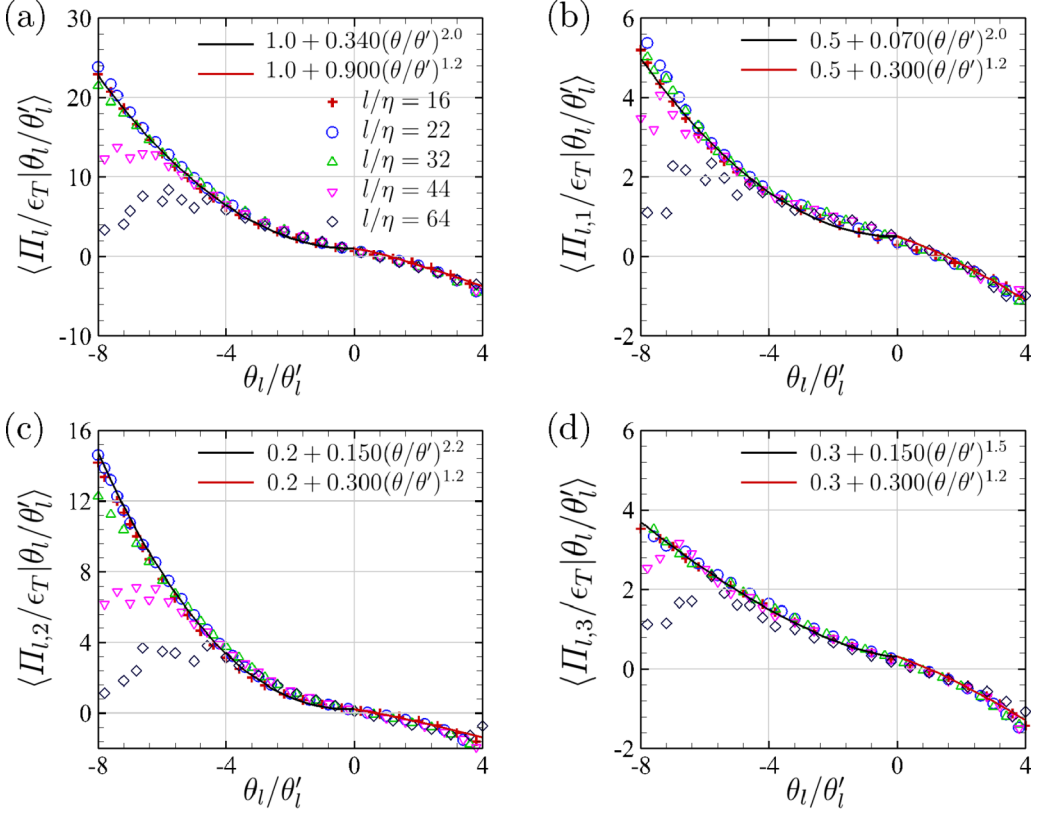
FIG. 23. Average of normalized SGS flux conditioned on the normalized filtered velocity divergence θ_l/θ_l' for different filter widths $l/\eta = 16, 22, 32, 44, 64$ at $M_t = 0.46$ and $\mathrm{Re}_\lambda = 156$. (a) $\langle \Pi_l/\epsilon_T | \theta_l/\theta_l' \rangle$, (b) $\langle \Pi_{l,1}/\epsilon_T | \theta_l/\theta_l' \rangle$, (c) $\langle \Pi_{l,2}/\epsilon_T | \theta_l/\theta_l' \rangle$, (d) $\langle \Pi_{l,3}/\epsilon_T | \theta_l/\theta_l' \rangle$.

models [in Eqs. (34) and (35)] fit $\langle \Pi_l/\epsilon_T | \theta_l/\theta_l' \rangle$ fairly well in the compression regions with $b = 1.0, \alpha_0 = 0.34, n = 2.0$ and in the expansion regions with $b = 1.0, \alpha_1 = 0.9, m = 1.2$ at $M_t = 0.46$ and $\mathrm{Re}_\lambda = 156$, as shown in Fig. 23(a). In the compression regions, the (b, α_0, n) are (0.5, 0.07, 2.0), (0.2, 0.15, 2.2), and (0.3, 0.15, 1.5) for $\langle \Pi_{l,i}/\epsilon_T | \theta_l/\theta_l' \rangle$ ($i = 1, 2, 3$), respectively.

The average of β_l conditioned on the normalized filtered velocity divergence θ_l/θ_l' for different filter widths $l/\eta = 16, 22, 32, 44, 64$ at $M_t = 0.46$ and $\mathrm{Re}_\lambda = 156$ is shown in Fig. 24. The conditional averages of β_l and $\beta_{l,i}$ for different filter widths collapse rather well to a single curve. It is found that $\langle \beta_{l,2} | \theta_l/\theta_l' \rangle$ is much closer to -1 than $\langle \beta_{l,1} | \theta_l/\theta_l' \rangle$ and $\langle \beta_{l,3} | \theta_l/\theta_l' \rangle$ when $\theta_l/\theta_l' < -5$, indicating the higher efficiency of interscale kinetic energy transfer in the vertical direction.

C. Helmholtz decomposition on SGS flux of kinetic energy

The rms fluctuations of the solenoidal velocity u^s and the dilatational velocity u^d are listed in Table III, as well as their three components. Both in FAT and in HST, the dilatational component contributes to a small fraction of the total kinetic energy. The rms fluctuation of u_i^s is similar with that of u_i (see Table II). It is interesting to find that $(u_i^d)'$ is isotropic in FAT, while it is obviously anisotropic in HST with more dilatational kinetic energy residing in the vertical direction, consistent with a previous numerical result by Livescu and Madnia [58].

The averages of the solenoidal production $\langle P_l^s \rangle/\epsilon_T$ and the dilatational production $\langle P_l^d \rangle/\epsilon_T$ are shown in Fig. 25 for HST. Both $\langle P_l^s \rangle/\epsilon_T$ and $\langle P_l^d \rangle/\epsilon_T$ are positive, indicating that the mean energy
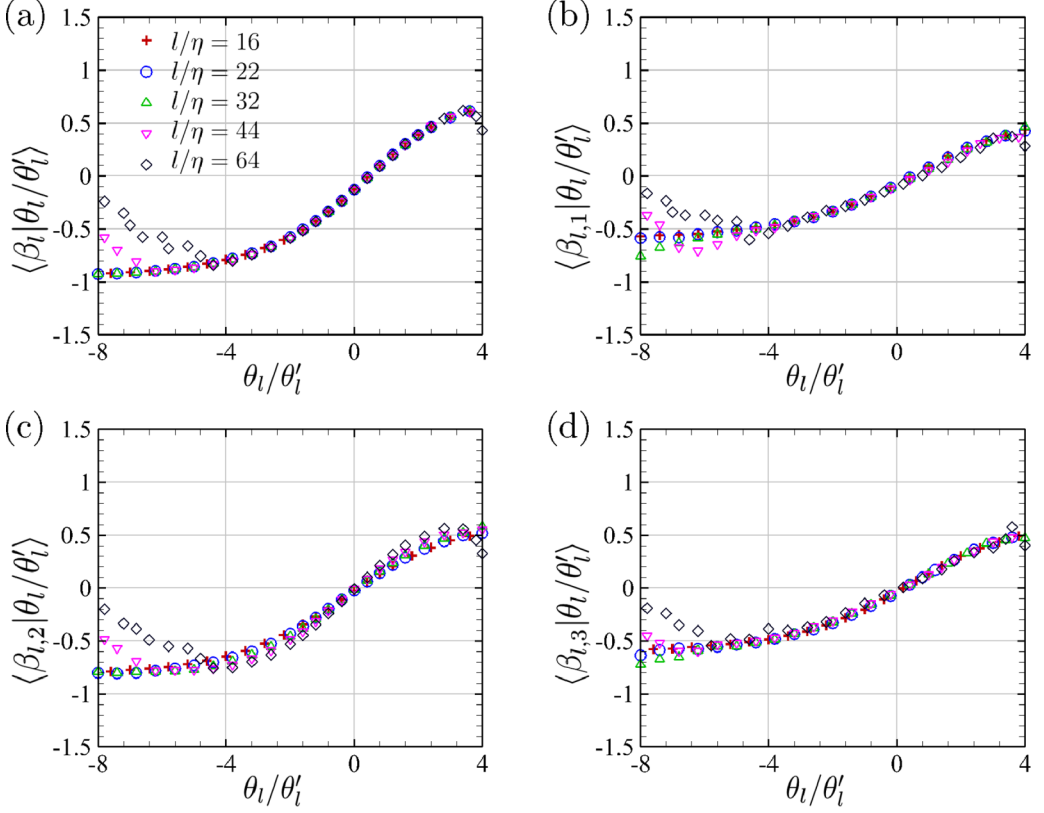
FIG. 24. Average of β_l conditioned on the normalized filtered velocity divergence θ_l/θ_l' for different filter widths $l/\eta = 16$ at $M_t = 0.46$ and $\mathrm{Re}_\lambda = 156$. (a) $\langle\beta_l|\theta_l/\theta_l'\rangle$, (b) $\langle\beta_{l,1}|\theta_l/\theta_l'\rangle$, (c) $\langle\beta_{l,2}|\theta_l/\theta_l'\rangle$, (d) $\langle\beta_{l,3}|\theta_l/\theta_l'\rangle$.

is transferred to turbulent kinetic energy not only from solenoidal mode but also from dilatational mode. The solenoidal production $\langle P_l^s\rangle/\epsilon_T$ is significantly larger than the dilatational production $\langle P_l^d\rangle/\epsilon_T$, probably leading to qualitative similarity of energy transfer between HST and FAT where

TABLE III. Component anisotropy statistics of dilatational velocity and solenoidal velocity.

| Flow type	Dilatational velocity components				Solenoidal velocity components			
	$(u^d)'/u'$	$(u_1^d)'/u'$	$(u_2^d)'/u'$	$(u_3^d)'/u'$	$(u^s)'/u'$	$(u_1^s)'/u'$	$(u_2^s)'/u'$	$(u_3^s)'/u'$
FAT1	0.15	0.09	0.09	0.09	0.99	0.89	0.30	0.30
FAT2	0.19	0.11	0.11	0.11	0.98	0.86	0.33	0.34
FAT3	0.20	0.12	0.12	0.12	0.98	0.83	0.36	0.36
FAT4	0.06	0.04	0.03	0.03	1.00	0.82	0.40	0.39
FAT5	0.13	0.08	0.08	0.07	0.99	0.80	0.41	0.41
FAT6	0.16	0.10	0.09	0.09	0.99	0.81	0.40	0.40
FAT7	0.19	0.11	0.11	0.11	0.98	0.84	0.35	0.36
FAT8	0.19	0.11	0.11	0.11	0.98	0.84	0.36	0.36
HST1	0.08	0.03	0.06	0.04	1.00	0.70	0.48	0.52
HST2	0.21	0.09	0.16	0.10	0.98	0.69	0.47	0.50
HST3	0.23	0.11	0.17	0.11	0.97	0.70	0.46	0.49
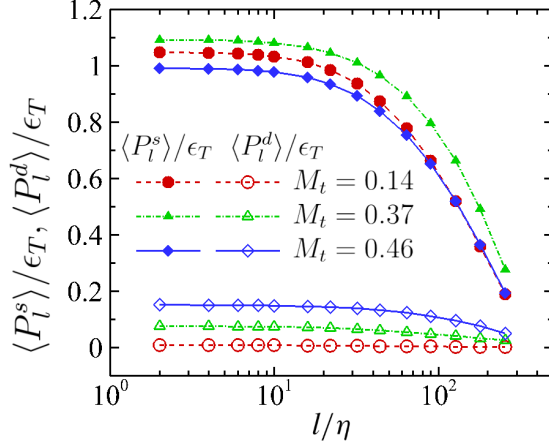
FIG. 25. Average of solenoidal and dilatational components of the production of HST. Solid line for $\langle P_l^s \rangle / \epsilon_T$ and dash-dotted line for $\langle P_l^d \rangle / \epsilon_T$.

the large-scale force is only applied to solenoidal component of the velocity field. We can see that $\langle P_l^d \rangle / \epsilon_T$ increases with the increasing turbulent Mach number, suggesting the enhancing of the production of dilatational kinetic energy by compressibility. Figure 26 displays the averages of the normalized solenoidal and dilatational components of the viscous dissipation: $\langle D_l^s \rangle / \epsilon_T$ and $\langle D_l^d \rangle / \epsilon_T$. The solenoidal viscous dissipation makes a major contribution to loss of kinetic energy at small scales. As turbulent Mach number increases, the normalized solenoidal viscous dissipation decreases, while the normalized dilatational viscous dissipation increases.

Figure 27 displays the average of the normalized solenoidal and dilatational components of the SGS kinetic energy flux: $\langle \Pi_l^s \rangle / \epsilon_T$ and $\langle \Pi_l^d \rangle / \epsilon_T$. For both FAT and HST, the solenoidal SGS flux $\langle \Pi_l^s \rangle / \epsilon_T$ makes a major contribution to the net transfer of kinetic energy from large scales to small scales in the range of $30 \leqslant l/\eta \leqslant 100$. The average dilatational SGS flux $\langle \Pi_l^d \rangle / \epsilon_T$ increases with turbulent Mach number, implying the enhancement effect of compressibility on the interscale transfer of dilatational kinetic energy. The observations are consistent with previous studies on compressible isotropic turbulence by Wang *et al.* [9]. The average solenoidal SGS flux $\langle \Pi_l^s \rangle / \epsilon_T$ is more affected by turbulent Mach number in HST, while it is nearly independent of turbulent Mach number in FAT and in HIT [9].
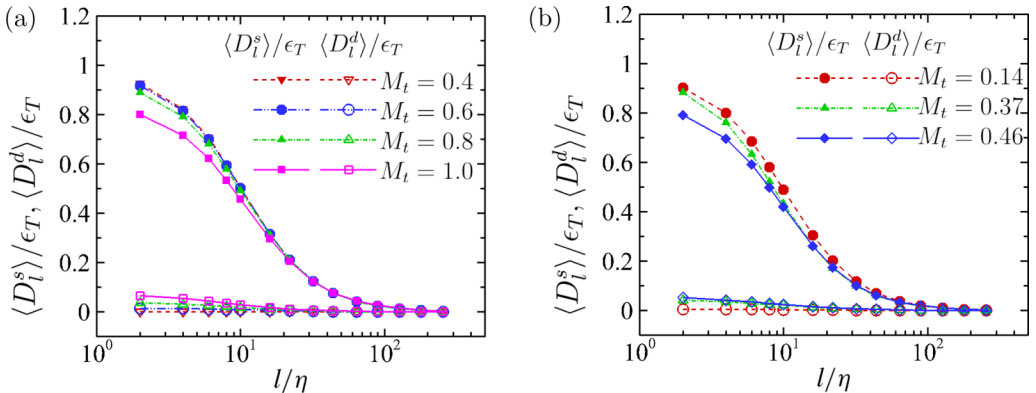

FIG. 26. Average of solenoidal and dilatational components of the viscous dissipation. (a) FAT and (b) HST.
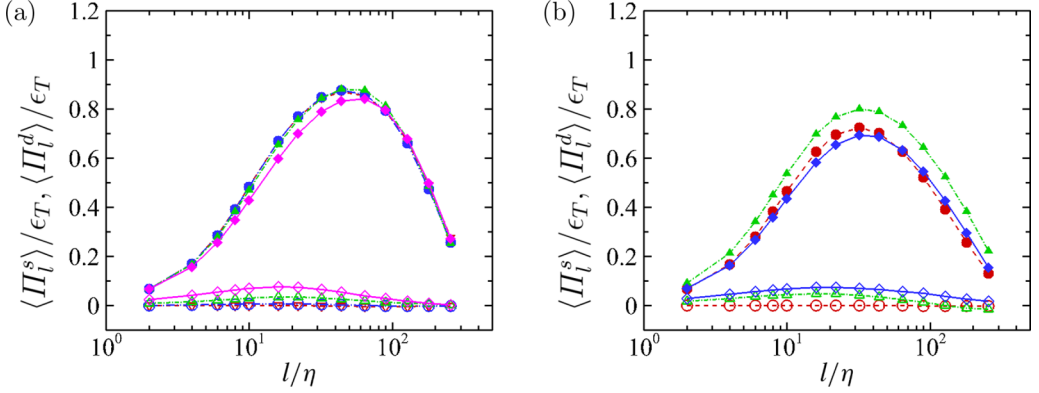
FIG. 27. Average of solenoidal and dilatational components of the SGS kinetic energy flux. (a) FAT and (b) HST. The legend is the same as in Fig. 26.

Figure 28 displays the average of solenoidal and dilatational components of the nonlinear advection: $\langle A_l^s \rangle / \epsilon_T$ and $\langle A_l^d \rangle / \epsilon_T$. Wang *et al.* [9] found that in solenoidally forced stationary compressible isotropic turbulence, the kinetic energy is transferred from the solenoidal mode to the dilatational mode by the nonlinear advection terms, $\langle A_l^s \rangle / \epsilon_T$ and $\langle A_l^d \rangle / \epsilon_T$, which are enhanced by the increase of turbulent Mach number. As shown in Fig. 28(a), the behavior of nonlinear advection in FAT is consistent with that in compressible isotropic turbulence by Wang *et al.* [9]. It is interesting to observe that the nonlinear advection in HST first increases at lower turbulent Mach numbers $M_t \leqslant 0.37$ and then decreases as the turbulent Mach number increases at higher turbulent Mach numbers $M_t > 0.37$. At the highest turbulent Mach number $M_t = 0.46$, the nonlinear advection of HST ($\langle A_l^d \rangle / \epsilon_T \approx 0.02$) is negligibly small as compared with the dilatational production ($\langle P_l^s \rangle / \epsilon_T \approx 0.15$), indicating that the dilatational mode is maintained by dilatational production. In FAT and HIT [9], $-\langle A_l^s \rangle / \epsilon_T$ and $\langle A_l^d \rangle / \epsilon_T$ increase with the decrease of filter width until the smallest one, but the growth rate in HST is almost zero at small filter width. The observations indicate that the dilatational mode absorbs energy from the solenoidal mode through the nonlinear advection at different length scales in FAT and HIT, while mainly at large length scales in HST.
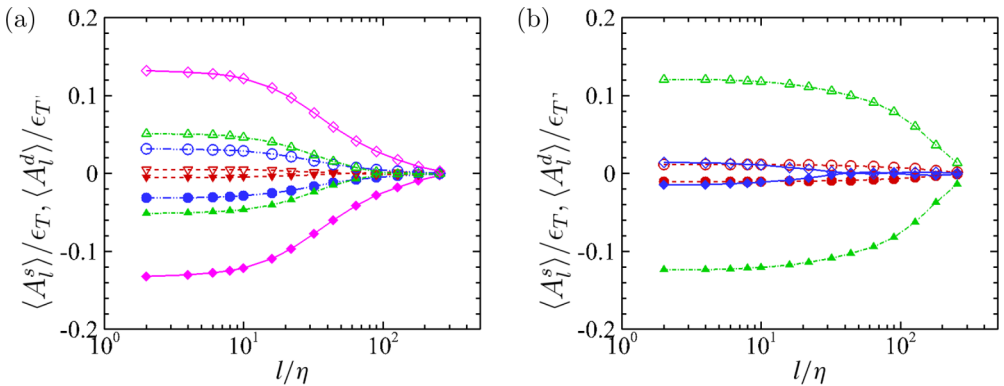

FIG. 28. Average of solenoidal and dilatational components of the nonlinear advection. (a) FAT and (b) HST. The legend is the same as in Fig. 26.

VI. CONCLUSION

In the present work, we have studied interscale and intercomponent kinetic energy transfer in stationary compressible FAT and HST with particular emphasis on the component anisotropy. A large-scale source of anisotropy is induced by large-scale streamwise external forcing and mean shear rate in FAT and HST, respectively. In both FAT and HST, the behaviors of transfer terms for total kinetic energy are quite consistent with a previous study on compressible isotropic turbulence by Wang *et al.* [9]. The SGS kinetic energy flux and viscous dissipation are dominated by the streamwise component at large scales, and tend to be isotropic at small scales. The recovery of local isotropy at small scales is incomplete due to the finite Taylor Reynolds number considered here. As turbulent Mach number increases, the compressibility slightly enhances the anisotropy of SGS flux and viscous dissipation. The average pressure-strain components redistribute energy from the streamwise direction to transverse directions, and this process mainly occurs at large length scales.

The anisotropy of SGS kinetic energy flux and viscous dissipation decreases rapidly with the increasing Taylor Reynolds number, but still exists at small scales up to $\mathrm{Re}_\lambda = 267$. As the Taylor Reynolds number increases, the total viscous dissipation and its streamwise component approach a Reynolds number asymptotic state, where a power-law decay is clearly observed at large scales. The total SGS kinetic energy flux is also found to be Reynolds number independent at high Taylor Reynolds number $\mathrm{Re}_\lambda \geqslant 105$, as well as its positive and negative components. Although the positive component of streamwise SGS flux is strongly dependent on Taylor Reynolds number, its negative component is nearly independent of Taylor Reynolds number.

In HST, large-scale Reynolds shear stress acts as the production of kinetic energy, whose effect is similar, but extends to much smaller scales as compared with that of large-scale external forcing in FAT. The streamwise energy loss by the pressure-strain is shared unequally by the other two components in HST. At high turbulent Mach numbers, the shape of the joint PDF of ($\Pi_{l,2}/\epsilon_T$, θ_l/θ_l') is much more asymmetric than those for $\Pi_{l,1}/\epsilon_T$ and $\Pi_{l,3}/\epsilon_T$, and dominated by the second quadrant. The enhancement of positive vertical SGS kinetic energy flux by compression motions is stronger than that of the two other components, causing the vertical SGS flux component $\langle \Pi_{l,2} \rangle$ to be larger than the streamwise component $\langle \Pi_{l,1} \rangle$ at small scales.

The interscale energy transfer of the solenoidal mode and dilatational mode is studied by employing Helmholtz decomposition. The dilatational production term in HST is nonzero and increases with the turbulent Mach number. In HST, kinetic energy transfer from the solenoidal mode to the dilatational mode by nonlinear advection occurs primarily at larger length scales as compared with that in FAT and HIT. The nonlinear advection term increases with turbulent Mach number in FAT and HIT, while it increases first and then decreases as the turbulent Mach number increases in HST, since the dilatational production provides more energy into the dilatational mode in HST.

[1] L. F. Richardson, *Weather Prediction by Numerical Process* (Cambridge University Press, Cambridge, 1922).

[2] A. N. Kolmogorov, The local structure of turbulence in incompressible viscous fluid for very large Reynolds numbers, Dokl. Akad. Nauk SSSR **30**, 299 (1941).

[3] S. B. Pope, *Turbulent Flows* (Cambridge University Press, Cambridge, 2000).

[4] R. Samtaney, D. I. Pullin, and B. Kosović, Direct numerical simulation of decaying compressible turbulence and shocklet statistics, Phys. Fluids **13**, 1415 (2001).

[5] S. Pirozzoli and F. Grasso, Direct numerical simulations of isotropic compressible turbulence: Influence of compressibility on dynamics and structures, Phys. Fluids **16**, 4386 (2004).

[6] J. Wang, Y. Shi, L.-P. Wang, Z. Xiao, X. He, and S. Chen, Effect of shocklets on the velocity gradients in highly compressible isotropic turbulence, Phys. Fluids **23**, 125103 (2011).

[7] J. Wang, Y. Shi, L.-P. Wang, Z. Xiao, X. T. He, and S. Chen, Effect of compressibility on the small-scale structures in isotropic turbulence, J. Fluid Mech. **713**, 588 (2012).

[8] Z. Ma and Z. Xiao, Turbulent kinetic energy production and flow structures in compressible homogeneous shear flow, Phys. Fluids **28**, 096102 (2016).

[9] J. Wang, M. Wan, S. Chen, and S. Chen, Kinetic energy transfer in compressible isotropic turbulence, J. Fluid Mech. **841**, 581 (2018).

[10] D. A. Donzis and J. P. John, Universality and scaling in homogeneous compressible turbulence, Phys. Rev. Fluids **5**, 084609 (2020).

[11] S. Kida and S. A. Orszag, Energy and spectral dynamics in decaying compressible turbulence, J. Sci. Comput. **7**, 1 (1992).

[12] H. Aluie, Compressible Turbulence: The Cascade and Its Locality, Phys. Rev. Lett. **106**, 174502 (2011).

[13] H. Aluie, S. Li, and H. Li, Conservative cascade of kinetic energy in compressible turbulence, Astrophys. J. Lett. **751**, L29 (2012).

[14] H. Aluie, Scale decomposition in compressible turbulence, Physica D **247**, 54 (2013).

[15] J. Wang, Y. Yang, Y. Shi, Z. Xiao, X. T. He, and S. Chen, Cascade of Kinetic Energy in Three-Dimensional Compressible Turbulence, Phys. Rev. Lett. **110**, 214505 (2013).

[16] J. Wang, M. Wan, S. Chen, C. Xie, Q. Zheng, L.-P. Wang, and S. Chen, Effect of flow topology on the kinetic energy flux in compressible isotropic turbulence, J. Fluid Mech. **883**, A11 (2020).

[17] M. K. Sharma, M. K. Verma, and S. Chakraborty, Anisotropic energy transfers in rapidly rotating turbulence, Phys. Fluids **31**, 085117 (2019).

[18] B. Teaca, M. K. Verma, B. Knaepen, and D. Carati, Energy transfer in anisotropic magnetohydrodynamic turbulence, Phys. Rev. E **79**, 046312 (2009).

[19] A. Alexakis, P. D. Mininni, and A. Pouquet, Shell-to-shell energy transfer in magnetohydrodynamics. I. Steady state turbulence, Phys. Rev. E **72**, 046301 (2005).

[20] A. Alexakis, B. Bigot, H. Politano, and S. Galtier, Anisotropic fluxes and nonlocal interactions in magnetohydrodynamic turbulence, Phys. Rev. E **76**, 056313 (2007).

[21] D. Chung and G. Matheou, Direct numerical simulation of stationary homogeneous stratified sheared turbulence, J. Fluid Mech. **696**, 434 (2012).

[22] C. Härtel, L. Kleiser, F. Unger, and R. Friedrich, Subgrid-scale energy transfer in the near-wall region of turbulent flows, Phys. Fluids **6**, 3130 (1994).

[23] D. C. Dunn and J. F. Morrison, Anisotropy and energy flux in wall turbulence, J. Fluid Mech. **491**, 353 (2003).

[24] C. M. Casciola, P. Gualtieri, R. Benzi, and R. Piva, Scale-by-scale budget and similarity laws for shear turbulence, J. Fluid Mech. **476**, 105 (2003).

[25] A. Cimarelli, E. De Angelis, and C. M. Casciola, Paths of energy in turbulent channel flows, J. Fluid Mech. **715**, 436 (2013).

[26] V. Borue and S. A. Orszag, Numerical study of three-dimensional Kolmogorov flow at high Reynolds numbers, J. Fluid Mech. **306**, 293 (1996).

[27] P. K. Yeung and J. G. Brasseur, The response of isotropic turbulence to isotropic and anisotropic forcing at the large scales, Phys. Fluids A **3**, 884 (1991).

[28] P. K. Yeung, J. G. Brasseur, and Q. Wang, Dynamics of direct large-small scale couplings in coherently forced turbulence: Concurrent physical- and Fourier-space views, J. Fluid Mech. **283**, 43 (1995).

[29] A. Alexakis, P. D. Mininni, and A. Pouquet, Imprint of Large-Scale Flows on Turbulence, Phys. Rev. Lett. **95**, 264503 (2005).

[30] L. Biferale and F. Toschi, Anisotropic Homogeneous Turbulence: Hierarchy and Intermittency of Scaling Exponents in the Anisotropic Sectors, Phys. Rev. Lett. **86**, 4831 (2001).

[31] L. Biferale, I. Daumont, A. Lanotte, and F. Toschi, Anomalous and dimensional scaling in anisotropic turbulence, Phys. Rev. E **66**, 056306 (2002).

[32] A. Pumir, Turbulence in homogeneous shear flows, Phys. Fluids **8**, 3112 (1996).

[33] A. Sekimoto, S. Dong, and J. Jiménez, Direct numerical simulation of statistically stationary and homogeneous shear turbulence and its relation to other shear flows, Phys. Fluids **28**, 035101 (2016).

[34] S. Dong, A. Lozano-Durán, A. Sekimoto, and J. Jiménez, Coherent structures in statistically stationary homogeneous shear turbulence, J. Fluid Mech. **816**, 167 (2017).

[35] H. Aluie and G. L. Eyink, Localness of energy cascade in hydrodynamic turbulence. II. Sharp spectral filter, Phys. Fluids **21**, 115108 (2009).

[36] J. I. Cardesa and A. Lozano-Durán, Inter-scale energy transfer in turbulence from the viewpoint of subfilter scales, Annual Research Briefs, Center for Turbulence Research, Stanford University, 1-15, 2019.

[37] S. Chen, J. Wang, H. Li, M. Wan, and S. Chen, Spectra and Mach number scaling in compressible homogeneous shear turbulence, Phys. Fluids **30**, 065109 (2018).

[38] W. Sutherland, LII. The viscosity of gases and molecular force, London, Edinb. Dublin Philos. Mag. J. Sci. **36**, 507 (1893).

[39] S. Chen, X. Wang, J. Wang, M. Wan, H. Li, and S. Chen, Effects of bulk viscosity on compressible homogeneous turbulence, Phys. Fluids **31**, 085115 (2019).

[40] J. Wang, L. Wang, Z. Xiao, Y. Shi, and S. Chen, A hybrid numerical simulation of isotropic compressible turbulence, J. Comput. Phys. **229**, 5257 (2010).

[41] D. S. Balsara and C. W. Shu, Monotonicity preserving weighted essentially non-oscillatory schemes with increasingly high order of accuracy, J. Comput. Phys. **160**, 405 (2000).

[42] S. K. Lele, Compact finite difference schemes with spectral-like resolution, J. Comput. Phys. **103**, 16 (1992).

[43] J. Wang, M. Wan, S. Chen, C. Xie, L.-P. Wang, and S. Chen, Cascades of temperature and entropy fluctuations in compressible turbulence, J. Fluid Mech. **867**, 195 (2019).

[44] R. S. Rogallo, *Numerical Experiments in Homogeneous Turbulence*, Tech. Rep. (NASA Ames Research Center, Moffett Field, CA, 1981).

[45] S. Chen, J. Wang, H. Li, M. Wan, and S. Chen, Effect of compressibility on small scale statistics in homogeneous shear turbulence, Phys. Fluids **31**, 025107 (2019).

[46] J. Wang, T. Gotoh, and T. Watanabe, Spectra and statistics in compressible isotropic turbulence, Phys. Rev. Fluids **2**, 013403 (2017).

[47] S. Jagannathan and D. A. Donzis, Reynolds and Mach number scaling in solenoidally-forced compressible turbulence using high-resolution direct numerical simulations, J. Fluid Mech. **789**, 669 (2016).

[48] F. H. Champagne, V. G. Harris, and S. Corrsin, Experiments on nearly homogeneous turbulent shear flow, J. Fluid Mech. **41**, 81 (1970).

[49] M. Lee and R. D. Moser, Direct numerical simulation of turbulent channel flow up to $Re_\tau \approx 5200$, J. Fluid Mech. **774**, 395 (2015).

[50] M. P. Martín, U. Piomelli, and G. V. Candler, Subgrid-scale models for compressible large-eddy simulations, Theor. Comput. Fluid Dyn. **13**, 361 (2000).

[51] H. Miura and S. Kida, Acoustic energy exchange in compressible turbulence, Phys. Fluids **7**, 1732 (1995).

[52] D. S. Praturi and S. S. Girimaji, Effect of pressure-dilatation on energy spectrum evolution in compressible turbulence, Phys. Fluids **31**, 055114 (2019).

[53] M. K. Verma, A. Kumar, P. Kumar, S. Barman, A. G. Chatterjee, R. Samtaney, and R. A. Stepanov, Energy spectra and fluxes in dissipation range of turbulent and laminar flows, Fluid Dyn. **53**, 862 (2018).

[54] M. K. Verma, *Energy Transfers in Fluid Flows: Multiscale and Spectral Perspectives* (Cambridge University Press, Cambridge, 2019).

[55] S. Lee, S. K. Lele, and P. Moin, Eddy shocklets in decaying compressible turbulence, Phys. Fluids A **3**, 657 (1991).

[56] F. Hamba, Effects of pressure fluctuations on turbulence growth in compressible homogeneous shear flow, Phys. Fluids **11**, 1623 (1999).

[57] X. Wang, S. Chen, J. Wang, H. Li, M. Wan, and S. Chen, Effect of compressibility on the local flow topology in homogeneous shear turbulence, Phys. Fluids **32**, 015118 (2020).

[58] D. Livescu and C. K. Madnia, Small scale structure of homogeneous turbulent shear flow, Phys. Fluids **16**, 2864 (2004).